ATLAS Paper Draft

ANA-HION-2018-03

Version 1.1

Target journal: Phys. Rev. C.

Comments are due by: 11 June 2019

Supporting internal notes

Correlations between jets and charged particles in Pb+Pb Collisions at 5.02 TeV:
https://cds.cern.ch/record/2304504

Measurement of angular and momentum distributions of charged particles within and around jets in Pb+Pb and pp collisions at $\sqrt{s_{\mathrm{NN}}} = 5.02$ TeV with the ATLAS detector

Studies of the fragmentation of jets into charged particles in heavy-ion collisions can provide information about the mechanism of jet quenching by the hot and dense QCD matter created in such collisions, the quark-gluon plasma. This paper presents a measurement of the angular distribution of charged particles around the jet axis in $\sqrt{s_{\mathrm{NN}}} = 5.02$ TeV Pb+Pb and pp collisions, done using the ATLAS detector at the LHC. The measurement is performed for jets reconstructed with the anti-k_t algorithm with radius parameter $R = 0.4$, and is extended to a distance of $r = 0.8$ from the jet axis. Results are presented as a function of Pb+Pb collision centrality and distance from the jet axis for charged particles with transverse momenta in the 1–63 GeV range, associated to jets with transverse momenta in the 126–316 GeV range within an absolute value of jet rapidity of less than 1.7. Modifications to the measured distributions are quantified by taking a ratio to the baseline measurements in pp collisions. Yields of charged particles with transverse momenta below 4 GeV are observed to be increasingly enhanced as a function of angular distance from the jet axis, achieving a maximum at $r = 0.6$. Charged particles with transverse momenta above 4 GeV have an enhanced yield in Pb+Pb collisions in the jet core for angular distances up to $r = 0.05$ from the jet axis, with a suppression at all larger distances.

Document created on 27th June 2019 using ATLAS LaTeX Version 07-02-00.

Analysis Team

[*email:* atlas-ana-hion-2018-03-analysis-team@cern.ch]

Akshat Puri, Anne Sickles, Martin Rybar

ATLAS Paper
ANA-HION-2018-03
27th June 2019
Journal: Phys. Rev. C.
Draft version 1.1

Measurement of angular and momentum distributions of charged particles within and around jets in Pb+Pb and pp collisions at $\sqrt{s_{\mathrm{NN}}} = 5.02$ TeV with the ATLAS detector

The ATLAS Collaboration

Studies of the fragmentation of jets into charged particles in heavy-ion collisions can provide information about the mechanism of jet quenching by the hot and dense QCD matter created in such collisions, the quark-gluon plasma. This paper presents a measurement of the angular distribution of charged particles around the jet axis in $\sqrt{s_{\mathrm{NN}}} = 5.02$ TeV Pb+Pb and pp collisions, done using the ATLAS detector at the LHC. The measurement is performed for jets reconstructed with the anti-k_t algorithm with radius parameter $R = 0.4$, and is extended to a distance of $r = 0.8$ from the jet axis. Results are presented as a function of Pb+Pb collision centrality and distance from the jet axis for charged particles with transverse momenta in the 1–63 GeV range, associated to jets with transverse momenta in the 126–316 GeV range within an absolute value of jet rapidity of less than 1.7. Modifications to the measured distributions are quantified by taking a ratio to the baseline measurements in pp collisions. Yields of charged particles with transverse momenta below 4 GeV are observed to be increasingly enhanced as a function of angular distance from the jet axis, achieving a maximum at $r = 0.6$. Charged particles with transverse momenta above 4 GeV have an enhanced yield in Pb+Pb collisions in the jet core for angular distances up to $r = 0.05$ from the jet axis, with a suppression at all larger distances.

1 Introduction

Ultra-relativistic nuclear collisions at the Large Hadron Collider (LHC) produce hot, dense matter called the quark-gluon plasma, QGP (see Refs. [1, 2] for recent reviews). Jets from hard-scattering processes in these collisions traverse and interact with the QGP, losing energy via a process called jet-quenching. The rates and characteristics of these jets in heavy-ion collisions can be compared to the same quantities in *pp* collisions, where we do not expect the production of QGP. This comparison can provide information on the properties of the QGP and how it interacts with partons from the hard scatter.

Jets with large transverse momenta in central lead-lead (Pb+Pb) collisions at the LHC are measured at approximately half the rates in *pp* collisions when the nuclear overlap function of Pb+Pb collisions is taken into account [3–7]. Similarly, back-to-back dijet [8–10] and photon-jet pairs [11, 12] are observed to have less balanced transverse momenta in Pb+Pb collisions compared to *pp* collisions. These observations suggest that some of the energy from the hard-scattered parton may be transferred outside of the jet through its interaction with the QGP medium.

Complementary measurements look at how the structure of jets is different between Pb+Pb and *pp* collisions. Jet shape measurements in the *pp* and Pb+Pb collision systems have shown a broadening of the jets due to the QGP [13–16]. Additionally, measurements of jet fragmentation functions at the LHC show an excess, in PbPb collisions, of low and high momentum particles with a depletion of intermediate momentum particles inside the jet compared to pp collisions [17–20]. Particles carrying a large fraction of the jet momentum are generally closely aligned with the jet axis, whereas low momentum particles are observed to have a much broader angular distribution extending outside the jet [9, 21–23]. These observations suggest that the energy lost via jet-quenching is being transferred to soft particles around the jet axis via soft gluon emission [24–30]. Measurements of yields of these particles as a function of transverse momentum and angular distance between the particle and the jet axis have a potential to provide further insight into on the structure of jets in the QGP, as well as provide information on how the medium is affected by the presence of the jet.

This paper presents charged-particle p_{T} distributions around the jet axis that have been corrected for detector effects. The measured yields are defined as:

$$D(p_{\mathrm{T}}, r) = \frac{1}{N_{\mathrm{jet}}} \frac{1}{A} \frac{\mathrm{d}n_{\mathrm{ch}}(p_{\mathrm{T}}, r)}{\mathrm{d}p_{\mathrm{T}}},$$

where $r = \sqrt{\Delta\eta^2 + \Delta\phi^2}$ [1] is the angular distance from the jet axis and N_{jet} is the number of jets in consideration. $A = \pi(r_{\max}^2 - r_{\min}^2)$ is the area of an annulus around the jet axis with its inner and outer radii $r_{\min}$ and $r_{\max}$ respectively and $n_{\mathrm{ch}}(p_{\mathrm{T}}, r)$ is the number of charged particles with a given p_{T} within the annulus. The ratios of the charged-particle yields measured in Pb+Pb and *pp* collisions,

[1] ATLAS uses a right-handed coordinate system with its origin at the nominal interaction point (IP) in the centre of the detector, and the z-axis along the beam pipe. The x-axis points from the IP to the centre of the LHC ring, and the y-axis points upward. Cylindrical coordinates (r, ϕ) are used in the transverse plane, ϕ being the azimuthal angle around the z-axis. The pseudorapidity is defined in terms of the polar angle θ as $\eta = -\ln\tan(\theta/2)$. The rapidity is defined as $y = 0.5\ln[(E + p_z)/(E - p_z)]$ where E and p_z are the energy and z-component of the momentum along the beam direction respectively. Transverse momentum and transverse energy are defined as $p_{\mathrm{T}} = p\sin\theta$ and $E_{\mathrm{T}} = E\sin\theta$, respectively. The angular distance between two objects with relative differences $\Delta\eta$ and $\Delta\phi$ in pseudorapidity and azimuth respectively is given by $\sqrt{(\Delta\eta)^2 + (\Delta\phi)^2}$.

$$R_{D(p_{\mathrm{T}},r)} = \frac{D(p_{\mathrm{T}},r)_{\mathrm{Pb+Pb}}}{D(p_{\mathrm{T}},r)_{pp}},$$

quantify the modifications of the yields due to the QGP medium. Furthermore, the differences between the $D(p_{\mathrm{T}},r)$ distributions in Pb+Pb and pp collisions,

$$\Delta D(p_{\mathrm{T}},r) = D(p_{\mathrm{T}},r)_{\mathrm{Pb+Pb}} - D(p_{\mathrm{T}},r)_{pp},$$

allow for measuring the absolute differences in charged-particle yields between the two collision systems.

2 ATLAS Detector

The measurements presented here are performed using the ATLAS calorimeter, inner detector, trigger, and data acquisition systems.

The calorimeter system consists of a sampling liquid-argon (LAr) electromagnetic (EM) calorimeter covering $|\eta| < 3.2$, a steel–scintillator sampling hadronic calorimeter covering $|\eta| < 1.7$, LAr hadronic calorimeters covering $1.5 < |\eta| < 3.2$, and two LAr forward calorimeters (FCal) covering $3.1 < |\eta| < 4.9$.

The EM calorimeters are segmented longitudinally in shower depth into three layers with an additional pre-sampler layer. They have segmentation that varies with layer and pseudorapidity. The hadronic calorimeters have three sampling layers longitudinal in shower depth [31].

The inner detector measures charged particles within the pseudorapidity interval $|\eta| < 2.5$ using a combination of silicon pixel detectors, silicon microstrip detectors (SCT), and a straw-tube transition radiation tracker (TRT), all immersed in a 2 T axial magnetic field [31]. Each of the three detectors is composed of a barrel and two symmetric end-cap sections. The pixel detector is composed of four layers including the Insertable B-Layer [32, 33]. The SCT barrel section contains four layers of modules with sensors on both sides, and each end-cap consists of nine layers of double-sided modules with radial strips. The TRT contains layers of staggered straws interleaved with the transition radiation material.

The zero-degree calorimeters (ZDCs) are located symmetrically at $z = \pm 140$ m and cover $|\eta| > 8.3$. The ZDCs use tungsten plates as absorbers, and quartz rods sandwiched between the tungsten plates as the active medium. In Pb+Pb collisions the ZDCs primarily measure "spectator" neutrons. These are neutrons that do not interact hadronically when the incident nuclei collide. A ZDC coincidence trigger is implemented by requiring the pulse height from both ZDCs to be above a threshold that accepts the signal corresponding to the energy deposition from a single neutron.

This analysis uses the same trigger setup used in Ref. [20], and is briefly described below. A two-level trigger system is used to select the Pb+Pb and pp collisions. The first level is based on custom electronics while the second level, the High Level Trigger (HLT), is based on software [34]. Minimum-bias (MB) events are recorded using a logical OR of two triggers: 1) total energy Level-1 trigger; 2) ZDC coincidence trigger at Level-1 and a veto on the total energy trigger, with the additional requirement of least one track in the HLT. The total-energy trigger requires a total transverse energy measured in the calorimeter system to be greater than 50 GeV. Jet events are selected by the HLT, seeded by a jet identified by the Level-1 jet trigger in pp collisions or by the total-energy trigger with a threshold of 50 GeV in Pb+Pb collisions. The Level-1 jet trigger utilized in pp collisions requires a jet with transverse momentum greater than 20 GeV. The HLT jet trigger uses a jet reconstruction procedure similar to that in the offline analysis as discussed in Section 4. It selects events containing jets with a transverse energy of at least 75 GeV in Pb+Pb collisions and at least 85 GeV in pp collisions. The measurement is performed in the jet transverse momentum range where the trigger is fully efficient.

3 Data sets and event selection

The Pb+Pb and pp data used in this analysis were recorded in 2015. The data samples consist of 25 pb^{-1} of $\sqrt{s}$ = 5.02 TeV pp and 0.49 nb^{-1} of $\sqrt{s_{\mathrm{NN}}}$ = 5.02 TeV Pb+Pb data. In both samples, events are required to have a reconstructed vertex within 150 mm of the nominal IP along the beam axis. The pileup is negligible in the Pb+Pb while the pp data is collected in low pileup mode. The average number of interactions per bunch crossing in pp collisions ranges from 0.6 to 1.3 [35]. Only events taken during stable beam conditions and satisfying detector and data-quality requirements that include the detector subsystems being in nominal operating conditions are considered.

The pp Monte Carlo (MC) used a set of 1.8×10^7 5.02 TeV hard-scattering dijet pp events generated with Powheg+Pythia8 [36, 37] using the A14 tune of parameters [38] and the NNPDF23LO PDF set [39].

The Pb+Pb MC was generated by overlaying an additional set of minimum bias Pb+Pb data events on a separate set of 1.8×10^7 5.02 TeV hard-scattering dijet pp events generated with the same tune and PDFs as the pp MC. This "MC overlay" sample is reweighted on an event-by-event basis such that it has the same centrality distribution as the jet triggered sample. The event centrality reflects the overlap area of the two colliding nuclei and is characterized by $\Sigma E_{\mathrm{T}}^{\mathrm{FCal}}$, the total transverse energy deposited in the FCal [40]. The six centrality intervals used in this analysis are defined according to successive percentiles of the $\Sigma E_{\mathrm{T}}^{\mathrm{FCal}}$ distribution obtained in MB collisions, ordered from the most central (highest $\Sigma E_{\mathrm{T}}^{\mathrm{FCal}}$) to the most peripheral (lowest $\Sigma E_{\mathrm{T}}^{\mathrm{FCal}}$) collisions: 0–10%, 10–20%, 20–30%, 30–40%, 40–60%, 60–80%. Another sample of MB Pb+Pb events was generated using HIJING (version 1.38b) [41] and was only used to evaluate the track reconstruction performance.

The detector response was simulated in both MC samples using Geant4 [42, 43] and was used to evaluate the performance of the detector and analysis procedure.

A weight is assigned to each MC event such that the event sample obtained from the simulation has the same $\Sigma E_{\mathrm{T}}^{\mathrm{FCal}}$ distribution as in jet triggered data.

4 Jet and track selection

The jet reconstruction procedure is identical to that used in Ref. [7]. The anti-k_t algorithm [44, 45] is first run in four-momentum recombination mode, on $\Delta\eta \times \Delta\phi = 0.1 \times 0.1$ calorimeter towers with two anti-k_t radius parameter values ($R = 0.2$ and $R = 0.4$). The energies in the towers are obtained by summing the energies of calorimeter cells at the electromagnetic energy scale. Then, an iterative procedure is used to estimate the η-dependent underlying event (UE) transverse energy density, while excluding the regions populated by jets. The estimate of the UE contribution is performed on an event-by-event basis. Furthermore, the background in Pb+Pb collisions is modulated to account for the azimuthal anisotropy in particle production [46]. The modulation includes the contributions of the second, third, and fourth order azimuthal anisotropy harmonics. The UE transverse energy is subtracted from calorimeter towers included in the jet and the four-momentum of the jet is updated accordingly. Then, a jet η- and p_{T}-dependent correction factor to the $p_{\mathrm{T}}^{\mathrm{jet}}$ derived from the pp MC is applied to correct for the calorimeter energy response [47]. The same calibration factors are applied both in pp and Pb+Pb collisions. An additional correction based on *in situ* studies of jets recoiling against photons, Z bosons, and jets in other regions of the calorimeter is applied [48, 49]. The same jet reconstruction procedure without the azimuthal modulation of the UE is also applied to pp collisions. Furthermore, the UE subtraction in pp collisions removes jet pileup effects. In this analysis, jets are required to have $p_{\mathrm{T}}^{\mathrm{jet}}$ in the 126–316 GeV range, with rapidity $|y^{\mathrm{jet}}| < 1.7$. The $p_{\mathrm{T}}^{\mathrm{jet}}$ cut is chosen so as to exclude the contribution of "UE jets" generated by fluctuations in the underlying event, while the rapidity cut is based on the acceptance of the tracking system. To prevent nearby jets from distorting the measurement of $D(p_{\mathrm{T}}, r)$ distributions, jets are rejected if there is a neighboring jet with higher $p_{\mathrm{T}}^{\mathrm{jet}}$ within an angular distance of $\Delta R < 1.0$. This isolation requirement removes approximately 0.01% of jets.

Charged-particle tracks in Pb+Pb collisions are reconstructed from hits in the inner detector using the track reconstruction algorithm that has been optimized for the high hit density in heavy-ion collisions [50]. Tracks used in this analysis have $|\eta| < 2.5$ and are required to have at least 9 (11) total hits in the pixel and SCT detectors for charged particles with pseudorapidity $|\eta^{\mathrm{ch}}| \leq 1.65$ ($|\eta^{\mathrm{ch}}| > 1.65$). At least one hit is required in one of the two innermost pixel layers. If the track trajectory passes through an active module in the innermost layer, then a hit in this layer is required. Additionally, a track must have no more than two holes in the pixel and SCT detectors together, where a hole is defined by the absence of a hit predicted by the track trajectory. All charged-particle tracks used in this analysis are required to have reconstructed transverse momentum $p_{\mathrm{T}}^{\mathrm{ch}} > 1.0$ GeV. In order to suppress a contribution from secondary particles[2], the distance of closest approach of the track to the primary vertex is required to be less than a value that varies from 0.45 mm at $p_{\mathrm{T}}^{\mathrm{ch}} = 4$ GeV to 0.2 mm at $p_{\mathrm{T}}^{\mathrm{ch}} = 20$ GeV in the transverse plane and is less than 1.0 mm in the longitudinal direction.

The efficiency, ε, for reconstructing charged particles in Pb+Pb and pp collisions is determined using the MC samples described above. It is evaluated as a function of the generator-level primary particle transverse momentum, $p_{\mathrm{T}}^{\mathrm{truth}}$, and pseudorapidity, η^{truth}, by associating tracks to generator-level primary particles [43]. In both collision systems the efficiency increases slowly with $p_{\mathrm{T}}^{\mathrm{truth}}$ and is seen to be independent of $p_{\mathrm{T}}^{\mathrm{jet}}$ in the measurement phase space. For Pb+Pb collisions, the efficiency for $|\eta| < 0.3$ is $\sim 80\%$ at 1 GeV and rises to $\sim 85\%$ at 10 GeV. For $1.0 < |\eta| < 2.0$, the efficiency is $\sim 67\%$ to $\sim 72\%$ over the same p_{T} range, with the variation in efficiency between the most central and peripheral Pb+Pb collisions being approximately 3% in both η ranges. For pp collisions, the efficiency for $|\eta| < 0.3$ is $\sim 85\%$ at 1 GeV, and rises to $\sim 88\%$ at 10 GeV, remaining relatively constant thereafter. For $1.0 < |\eta| < 2.0$, the efficiency is $\sim 82\%$ to $\sim 86\%$ over the same p_{T} range. Further details on the tracking efficiency can be found in Ref. [19].

The contribution of reconstructed tracks that cannot be matched to a generated primary particle in the pp MC samples is less than 2% in the entire $p_{\mathrm{T}}^{\mathrm{ch}}$ range under study in both pp and Pb+Pb collisions. This contribution includes fakes and secondaries, where fakes can be described as randomly associated hits in the detector layers that do not correspond to the passage of charged particles. Both these contributions are corrected for as described in the next section.

[2] Primary particles are defined as particles with a mean lifetime $\tau > 0.3 \times 10^{-10}$ s either directly produced in pp interactions or from subsequent decays of particles with a shorter lifetime.All other particles are considered to be secondary.

5 Analysis procedure

The analysis procedure is similar to that in Ref. [20] with the additional requirement of being done differentially in r. Measured tracks are associated with a reconstructed jet if they fall within a distance of 0.8 of the jet axis and the multiplicity distribution is given by:

$$\frac{\mathrm{d}^2 n_{\mathrm{ch}}^{\mathrm{meas}}}{\mathrm{d}p_{\mathrm{T}}^{\mathrm{ch}}\mathrm{d}r} = \frac{1}{\varepsilon(p_{\mathrm{T}}^{\mathrm{ch}}, \eta^{\mathrm{ch}})} \frac{\Delta n_{\mathrm{ch}}(p_{\mathrm{T}}^{\mathrm{ch}}, r)}{\Delta p_{\mathrm{T}}^{\mathrm{ch}} \Delta r}$$

where $\Delta n_{\mathrm{ch}}(p_{\mathrm{T}}^{\mathrm{ch}}, r)$ represents the number of tracks within a given $\Delta p_{\mathrm{T}}^{\mathrm{ch}}$ and Δr range. The efficiency correction is applied as a $1/\varepsilon(p_{\mathrm{T}}^{\mathrm{ch}}, \eta^{\mathrm{ch}})$ weight on a track-by-track basis, assuming $p_{\mathrm{T}}^{\mathrm{ch}} = p_{\mathrm{T}}^{\mathrm{truth}}$. While that assumption is not strictly valid, the efficiency varies sufficiently slowly with $p_{\mathrm{T}}^{\mathrm{truth}}$ that the error introduced by this assumption is less than 1%. It is further corrected for by the Bayesian unfolding procedure described later in this section.

The measured track yields need to be corrected for the UE, fake tracks and secondaries. In pp collisions, the UE contribution from hard scatterings not associated with jet production is negligible. The contributions from fake tracks and secondary charged particles are estimated from MC samples and subtracted. This procedure is similar to that applied in previous measurements [20, 35].

For Pb+Pb collisions, the UE, fake track, and secondary contributions are estimated together in a two step process: first, the MC overlay is used to generate η^{jet}vs. ϕ^{jet} maps of the average number of charged particles in a given annulus around a reconstructed jet. This is done for charged particles without a truth match and as a function of $p_{\mathrm{T}}^{\mathrm{jet}}$, η^{jet}, ϕ^{jet}, $\Delta\Psi_{\mathrm{jet}}$, r, $p_{\mathrm{T}}^{\mathrm{ch}}$, and centrality. Here $\Delta\Psi_{\mathrm{jet}}$ is the azimuthal angle of the jet to the second order event plane Ψ_2 and is given by $\Delta\Psi_{\mathrm{jet}} = \phi^{\mathrm{jet}} - \Psi_2$[3]. In the second step, the η^{jet}vs. ϕ^{jet} maps are used to generate the UE distribution as a function of $p_{\mathrm{T}}^{\mathrm{jet}}$, η^{jet}, ϕ^{jet}, and $\Delta\Psi_{\mathrm{jet}}$. This distribution includes fakes, and is given by $\mathrm{d}^2 {n_{\mathrm{ch}}}^{\mathrm{UE+Fake}}(p_{\mathrm{T}}^{\mathrm{ch}}, r)/\mathrm{d}p_{\mathrm{T}}^{\mathrm{ch}}\mathrm{d}r$. The yields decrease with decreasing collision centrality, increasing $p_{\mathrm{T}}^{\mathrm{ch}}$, and increasing $\Delta\Psi_2$. The subtracted distributions are then given by:

$$\frac{\mathrm{d}^2 n_{\mathrm{ch}}^{\mathrm{sub}}(r)}{\mathrm{d}p_{\mathrm{T}}^{\mathrm{ch}}\mathrm{d}r} = \frac{\mathrm{d}^2 n_{\mathrm{ch}}^{\mathrm{meas}}(r)}{\mathrm{d}p_{\mathrm{T}}^{\mathrm{ch}}\mathrm{d}r} - \frac{\mathrm{d}^2 {n_{\mathrm{ch}}}^{\mathrm{UE+Fake}}(r)}{\mathrm{d}p_{\mathrm{T}}^{\mathrm{ch}}\mathrm{d}r}.$$

Figure 1 shows the ratio of the charged-particle distributions before and after the subtraction of the UE, fake tracks, and secondaries, as a function of r for different $p_{\mathrm{T}}^{\mathrm{ch}}$ intervals and $126 < p_{\mathrm{T}}^{\mathrm{jet}} < 158$ GeV for six centrality selections. The largest UE contribution is for 1.0 GeV charged particles at large values of r in central collisions, with the background being approximately 100 times the signal, and slowly decreasing with increasing $p_{\mathrm{T}}^{\mathrm{jet}}$. It rapidly decreases for more peripheral collisions, larger $p_{\mathrm{T}}^{\mathrm{ch}}$ and smaller r.

To remove the effects of the bin migration due to the jet energy and track momentum resolution, the subtracted $\mathrm{d}^2 n_{\mathrm{ch}}^{\mathrm{sub}}/\mathrm{d}p_{\mathrm{T}}^{\mathrm{ch}}\mathrm{d}r$ distributions are corrected by a two-dimensional Bayesian unfolding [51] in $p_{\mathrm{T}}^{\mathrm{ch}}$ and $p_{\mathrm{T}}^{\mathrm{jet}}$ as implemented in the RooUnfold package [52]. Two-dimensional unfolding is used because the calorimetric jet energy response depends on the fragmentation pattern of the jet [53]. Four-dimensional response matrices are created from the pp and Pb+Pb MC samples using the generator-level and reconstructed $p_{\mathrm{T}}^{\mathrm{jet}}$ and

[3] The second order event plane angle Ψ_2 is determined on an event-by-event basis by a standard method using the ϕ variation of transverse energy in the FCal [46].

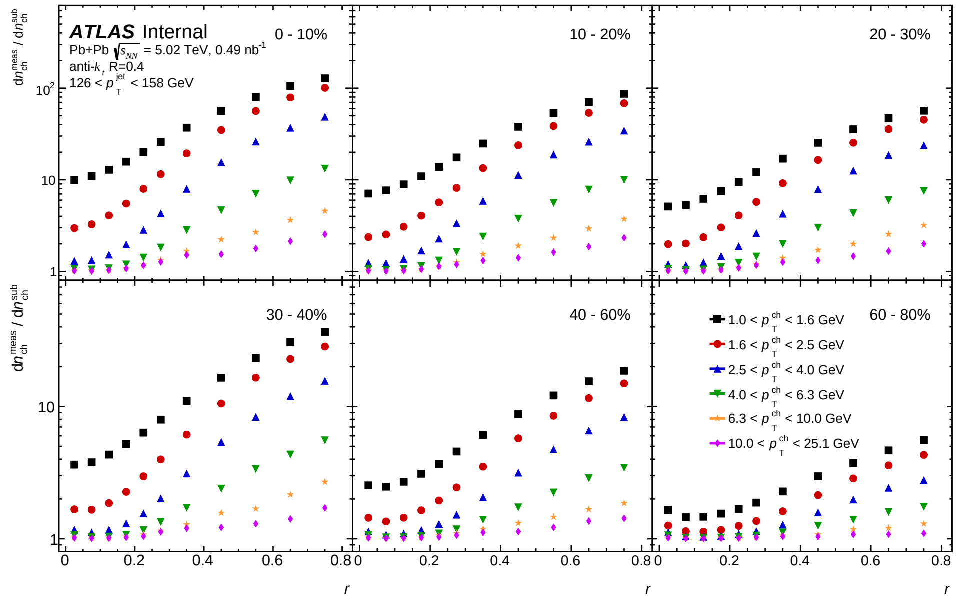

Figure 1: Ratio of the measured charged-particle distributions to those after the subtraction of the UE, fake tracks, and secondaries as a function of r for different p_T^{ch} intervals for p_T^{jet} between 126–158 GeV. The different panels represent the six centrality selections.

the generator-level and reconstructed charged-particle p_T^{ch}. They are corrected for tracking efficiencies and are evaluated in bins of r and centrality. The Bayesian procedure requires a choice in the number of iterations. Additional iterations reduce the sensitivity to the choice of prior, but may amplify statistical fluctuations in the distributions. After four iterations the charged-particle distributions are found to be stable within 2-4% for both the Pb+Pb and pp data. A separate one-dimensional Bayesian unfolding is used to correct the measured p_T^{jet} spectra that are used to normalize the unfolded charged-particle distributions. The response matrices for both the one and two dimensional unfolding are reweighted such that the charged-particle and jet distributions match the shapes of the analogous distributions in the reconstructed data.

An independent bin-by-bin unfolding procedure is also used to correct for migrations originating from the jet and track angular resolutions. Two corresponding $D(p_T, r)$ distributions are evaluated in MC samples, one using truth jets[4] and primary particles and the other using reconstructed jets and charged particles with their reconstructed p_T replaced by generator-level transverse momentum, p_T^{truth}. The ratio of these two MC distributions provides a correction factor which is then applied to the data. These factors are at the level of approximately 5% with variations up to 15% for particles with $p_T > 4$ GeV, particularly near the jet edge.

The final particle-level corrected distributions, normalized by the area of the annulus under question are defined as:

$$D(p_T, r) = \frac{1}{N_{jet}^{unfolded}} \frac{1}{A(r)} \frac{d^2 n_{ch}^{unfolded}(r)}{dp_T},$$

[4] Truth jets are reconstructed by applying the anti-k_t algorithm to stable final-state particles from MC generators like Pythia. Particles are required to have a lifetime of $c\tau > 10$ mm and muons, neutrinos, and particles from pile-up activity are excluded.

where $N_{\mathrm{jet}}^{\mathrm{unfolded}}$ is the unfolded number of jets in a given $p_{\mathrm{T}}^{\mathrm{jet}}$ interval, and $n_{\mathrm{ch}}^{\mathrm{unfolded}}$ is the unfolded yield of charged particles with a given p_{T} associated to a jet with given $p_{\mathrm{T}}^{\mathrm{jet}}$, within an annulus of area A at a distance r.

The performance of the full analysis procedure is validated in the MC samples by comparing the fully corrected charged-particle distributions to the generator-level distributions. We observe a good recovery of the generator-level distributions (closure) with a variation of less than 4% for charged particles with $p_{\mathrm{T}} < 10$ GeV in both the pp and Pb+Pb collision systems. The non-closure is taken as an additional systematic uncertainty as discussed in Section 6. It is to be noted that adding or removing particles carrying a large fraction of the jet momentum near the edge of the jet can significantly alter its reconstructed momentum and direction; this instability contributes to the non-closure mentioned above for particles with $p_{\mathrm{T}} > 10$ GeV in jets with $p_{\mathrm{T}}^{\mathrm{jet}} < 200$ GeV. Results are presented only where the non-closure in the pp MC sample is less than 5%.

6 Systematic uncertainties

The following sources of systematic uncertainty are considered: the jet energy scale (JES), the jet energy resolution (JER), the sensitivity of the unfolding to the prior, the UE contribution, the residual non-closure of the analysis procedure, and tracking-related uncertainties. For each systematic variation, the $D(p_{\mathrm{T}}, r)$ distributions along with their ratios and differences are re-evaluated. The difference between the varied and nominal distributions is used as an estimate of the uncertainty.

The systematic uncertainty due to the JES in Pb+Pb collisions is due to jets having a different structure and possibly a different detector response that is not modeled by the MC. It is composed of two parts: a centrality-independent baseline component and a centrality-dependent component. Only the centrality-independent baseline component is used in pp collisions; it is determined from *in situ* studies of the calorimeter response [47, 53, 54] and the relative energy scale difference between the jet reconstruction procedures in heavy-ion [54] and pp collisions [55]. The centrality-dependent uncertainty reflects a modification of parton showers by the Pb+Pb environment. It is evaluated by comparing calorimeter $p_{\mathrm{T}}^{\mathrm{jet}}$ and the vectorial sum of the transverse momentum of charged particles within the jet in data and MC. The size of the centrality-dependent uncertainty on the JES reaches 0.5% in the most central collisions. Each component that contributes to the JES uncertainty is varied separately by ± 1 standard deviation for each interval in $p_{\mathrm{T}}^{\mathrm{jet}}$ and the response matrix is recomputed accordingly. The data are then unfolded with the modified matrices. The resulting uncertainty from the JES increases with increasing charged-particle p_{T} at fixed $p_{\mathrm{T}}^{\mathrm{jet}}$ and decreases with increasing $p_{\mathrm{T}}^{\mathrm{jet}}$, and is at the level of 2–4%.

The uncertainty on the $D(p_{\mathrm{T}}, r)$ distributions due to the JER is evaluated by repeating the unfolding procedure with modified response matrices, where an additional contribution is added to the resolution of the reconstructed $p_{\mathrm{T}}^{\mathrm{jet}}$ using a Gaussian smearing procedure. The smearing factor is evaluated using an *in situ* technique in 13 TeV pp data that involves studies of dijet energy balance [56, 57]. An additional uncertainty is included to account for differences between the tower-based jet reconstruction and that used in analyses of 13 TeV pp data. The resulting uncertainty from the JER is symmetrized to account for negative variations of the JER. The size of the resulting uncertainty on the $D(p_{\mathrm{T}}, r)$ distributions due to the JER typically reaches 4–5% for the highest charged-particle p_{T} intervals and decreases to 2–3% with decreasing charged-particle p_{T} at fixed $p_{\mathrm{T}}^{\mathrm{jet}}$.

The uncertainties related to track reconstruction and selection originate from several sources. Uncertainties related to the material description in simulation and the track transverse momentum resolution are obtained from studies in data and simulation described in Ref. [58]. The sensitivity of the tracking efficiency to the description of the inactive material in the MC samples is evaluated by varying the material description. This resulting uncertainty in the track reconstruction efficiency is between 0.5% and 2% in the track p_{T} range used in the analysis. The systematic uncertainty on the fakes and secondaries is 30% in both collision systems [58]. The contamination of fake tracks is less than 2% and the resulting uncertainty in the $D(p_{\mathrm{T}}, r)$ distributions is at most 5%. An additional uncertainty takes into account a possible residual misalignment of the tracking detectors in pp and Pb+Pb data-taking. The alignment in these datasets is checked *in situ* with $Z \rightarrow \mu^{+}\mu^{-}$ events, and the track-p_{T} dependent uncertainty arises from the finite size of this sample. The resulting uncertainties in the $D(p_{\mathrm{T}}, r)$ distributions are typically less than 0.1%. An additional uncertainty in the tracking efficiency due to the high local track density in the core of jets is 0.4% [59] for all $p_{\mathrm{T}}^{\mathrm{jet}}$ ranges in this analysis. The uncertainty due to the track selection is evaluated by repeating the analysis with an additional 3σ cut on the significance of the distance of closest approach of the track to the primary vertex. This uncertainty affects the track reconstruction efficiencies, track momentum resolution, and rate of fake tracks. The resulting uncertainty typically varies between 1–2%. Finally, the track-to-particle association requirements are varied. This variation affects the track reconstruction efficiency, track momentum resolution, and rate of fake tracks. The resulting systematic uncertainty is $\leq$ 0.1% on the $D(p_{\mathrm{T}}, r)$ distributions. All track-related systematic uncertainties are added in quadrature and presented as the total tracking uncertainty.

The systematic uncertainty associated with the UE subtraction has two components: limited statistics of charged particles associated with a jet without a corresponding generator particle in the Pb+Pb MC Overlay, and a comparison to an alternative UE estimation done using the cone method. The cone method uses jet triggered events to estimate the background and is adapted from Refs. [19, 20]. A regular grid of 9 cones of size $R = 0.8$ is used to cover the inner detector region. Cones are excluded if they are within an angular distance of 1.6 to a reconstructed jet with $p_{\mathrm{T}}^{\mathrm{jet}} > 90$ GeV or if they contain a charged particle with $p_{\mathrm{T}} > 10$ GeV. This exclusion reduces biases from any hard processes. The resulting UE charged particle yields $\mathrm{d}n_{\mathrm{ch}}^{\mathrm{UE}^{\mathrm{Cone}}}/\mathrm{d}p_{\mathrm{T}}^{\mathrm{ch}}$ are evaluated over the 1–10 GeV range as a function of $p_{\mathrm{T}}^{\mathrm{ch}}$, $p_{\mathrm{T}}^{\mathrm{jet}}$, centrality, and r, and are subsequently averaged over all cones. Both of these sources of uncertainty combined as uncorrelated uncertainties. The combined UE uncertainty on the $D(p_{\mathrm{T}}, r)$ distributions is less than 10% for $r < 0.4$ and sharply decreases with increasing charged-particle p_{T}. It reaches a maximum of 40% at the largest angular distances from the jet axis and is the dominant source of the systematic uncertainty for low p_{T} charged-particles at large r. This is because of the small signal to background ratio at large distances from the jet axis. In particular, the component from the limited statistics dominates in the most central collisions, while the component from the alternative estimation method dominates elsewhere.

The systematic uncertainty on the unfolding procedure is estimated by generating response matrices from the MC distributions without the reweighting that matched the shapes of the charged-particle and jet distributions in data. The difference between the nominal $D(p_{\mathrm{T}}, r)$ distribution and that unfolded with the un-reweighted response matrix is taken as the systematic uncertainty, and is 5–7%.

An additional uncertainty to account for possible residual limitations in the analysis procedure is assigned by evaluating the non-closure of the unfolded distributions in simulations. This is typically at the level of 4%.

The correlations between the various systematic components are considered in evaluating the $R_{D(p_{\mathrm{T}},r)}$ and $\Delta D(p_{\mathrm{T}}, r)$ distributions. The unfolding and non-closure uncertainties are taken to be uncorrelated between

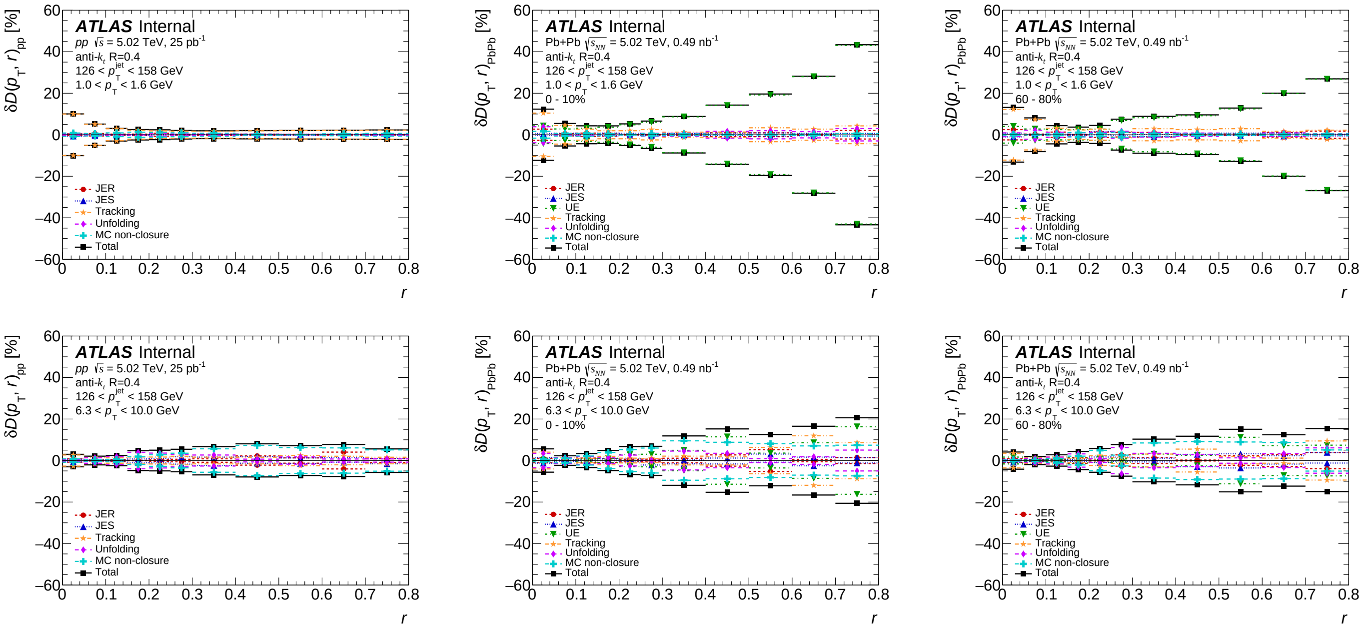

Figure 2: Relative size of the systematic uncertainties for $D(p_T, r)$ distributions in pp (left), central 0–10% Pb+Pb (middle), and peripheral 60–80% Pb+Pb (right) collisions for tracks with $1.0 < p_T < 1.6$ GeV (top) and $6.3 < p_T < 10$ GeV (bottom) in jets with $126 < p_T^{jet} < 158$ GeV. The systematic uncertainties due to JER, JES, UE, tracking, unfolding, and MC non-closure are shown along with the total systematic uncertainty from all sources.

pp and Pb+Pb collisions, while all others are taken to be correlated. For these, the $R_{D(p_T,r)}$ and $\Delta D(p_T, r)$ distributions are re-evaluated by applying the variation to both collision systems; the resulting variations of the ratios from their central values are used as the correlated systematic uncertainty.

Examples of systematic uncertainties in the $D(p_T, r)$ distributions for jets in the 126–158 GeV p_T^{jet} range measured in pp and Pb+Pb collision systems are shown in Figure 2. The uncertainties on the $R_{D(p_T,r)}$ distributions are shown in Figure 3. It can be seen that the dominant systematic uncertainty on the Pb+Pb and the $R_{D(p_T,r)}$ distributions is from the UE subtraction. While it is less than 5% for $r < 0.3$, it is approximately 40% for charged particles with $p_T = 1$ GeV at $r = 0.8$. The uncertainties in the pp system are smaller with the dominant systematic uncertainty at low p_T being due to the tracking. This is approximately 10% for $r < 0.1$ and decreases to less than 5% at larger distances.

7 Results

The $D(p_T, r)$ distributions are studied as a function of p_T^{jet} for pp data and Pb+Pb collisions with different centralities. The interplay between the hot and dense matter and the parton shower is explored by evaluating the ratios and differences between $D(p_T, r)$ distributions in Pb+Pb and pp collisions, as well as some integrated quantities.

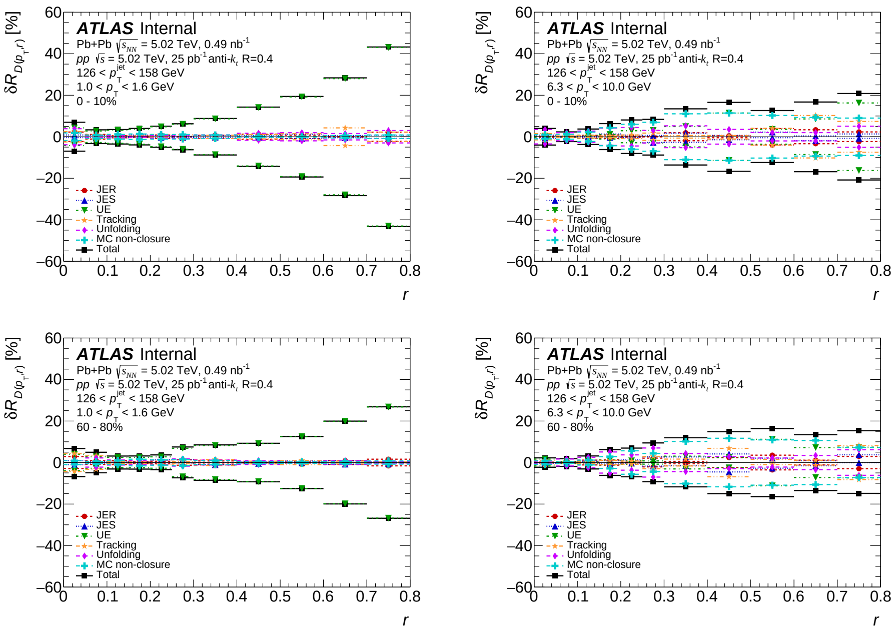

Figure 3: Relative size of the systematic uncertainties for $R_{D(p_{\mathrm{T}},r)}$ distributions for 0–10% (top) and 60–80% (bottom) Pb+Pb collisions, for tracks with $1.0 < p_{\mathrm{T}} < 1.6$ GeV (left) and $6.3 < p_{\mathrm{T}} < 10.0$ GeV (right), in jets with $126 < p_{\mathrm{T}}^{\mathrm{jet}} < 158$ GeV. The systematic uncertainties due to JES, JER, unfolding, UE contribution, MC non-closure, and tracking are shown along with the total systematic uncertainty from all sources.

7.1 $D(p_{\mathrm{T}}, r)$distributions

The $D(p_{\mathrm{T}}, r)$ distributions evaluated in pp and Pb+Pb collisions for $126 < p_{\mathrm{T}}^{\mathrm{jet}} < 158$ GeV are shown in Figure 4. The distributions exhibit a difference in shape between Pb+Pb and pp collisions, with the Pb+Pb distributions being broader at low p_{T} ($p_{\mathrm{T}} < 4$ GeV) and narrower at high p_{T} ($p_{\mathrm{T}} > 4$ GeV) in 0–10% central collisions. This modification is centrality dependent and is smaller for peripheral Pb+Pb collisions.

7.2 $R_{D(p_{\mathrm{T}},r)}$ distributions

In order to quantify the differences seen in Figure 4, ratios of the $D(p_{\mathrm{T}}, r)$ distributions in Pb+Pb collisions to those measured in pp collisions for $126 < p_{\mathrm{T}}^{\mathrm{jet}} < 158$ GeV and $200 < p_{\mathrm{T}}^{\mathrm{jet}} < 251$ GeV jets are presented in Figure 5. They are shown as a function of r for different p_{T} and centrality selections. In 0–10% central collisions, $R_{D(p_{\mathrm{T}},r)}$ is greater than unity for $r < 0.8$ for charged particles with p_{T} less than 4.0 GeV in both jet selections. For these particles, the enhancement of yields in Pb+Pb collisions compared to those in pp collisions grows with increasing r up to approximately $r = 0.3$, with $R_{D(p_{\mathrm{T}},r)}$ reaching up to two for $1.0 < p_{\mathrm{T}} < 2.5$ GeV. The value of $R_{D(p_{\mathrm{T}},r)}$ is approximately constant for r in the interval 0.3–0.6 and decreases for $r > 0.6$. For charged particles with $p_{\mathrm{T}} > 4.0$ GeV, $R_{D(p_{\mathrm{T}},r)}$ shows a depletion outside the jet core for $r > 0.05$. The magnitude of this depletion increases with increasing r up to $r = 0.3$ and is approximately constant thereafter. The observed behavior inside the jet cone, $r < 0.4$, agrees with the measurement of the inclusive jet fragmentation functions [10, 19, 20], where yields of fragments with $p_{\mathrm{T}} < 4$ GeV are observed to be enhanced and yields of charged particles with intermediate p_{T} are suppressed in Pb+Pb collisions compared to those in pp collisions. For 30–40% mid-central collisions,

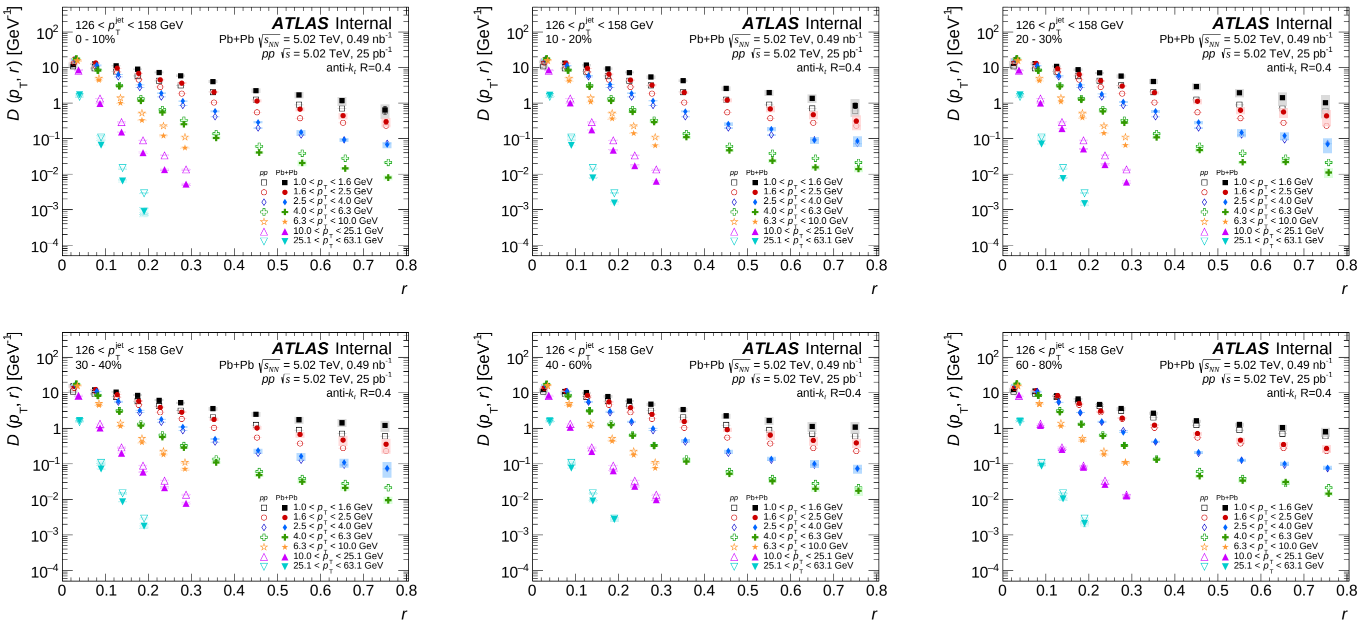

Figure 4: The $D(p_T, r)$ distributions in pp (open symbols) and Pb+Pb (closed symbols) as a function of angular distance r for p_T^{jet} of 126 to 158 GeV. The colors represent different track p_T ranges, and each panel is a different centrality selection. The vertical bars on the data points indicate statistical uncertainties while the shaded boxes indicate systematic uncertainties. The widths of the boxes are not indicative of the bin size and the points are shifted horizontally for better visibility. The distributions for $p_T > 6.3$ GeV are restricted to smaller r values as discussed in Section 5.

the enhancement of particles with $p_T < 4.0$ GeV is similar to that in the most central collisions, however the depletion of particles with $p_T > 4.0$ GeV is not as strong. For 60–80% peripheral collisions, $R_{D(p_T,r)}$ has no significant r dependence and the values of $R_{D(p_T,r)}$ are within approximately 50% of unity. The variation of $R_{D(p_T,r)}$ with centrality, p_T^{jet}, and charged-particle p_T is further discussed.

***$R_{D(p_T,r)}$* and centrality:** The centrality dependence of $R_{D(p_T,r)}$ for two charged-particle p_T intervals: 1.6–2.5 GeV and 6.3–10.0 GeV, and two different p_T^{jet} ranges: 126–158 GeV and 200–251 GeV, is presented in Figure 6. For both p_T^{jet} selections and 1.6–2.5 GeV charged particles, the magnitude of the excess increases for more central events and for r for $r < 0.3$. The magnitude of the excess is approximately a factor of two in the most central collisions for $r > 0.3$. A continuous centrality dependent suppression of yields of charged particles with $6.3 < p_T < 10.0$ GeV is observed. The magnitude of the modifications decreases for more peripheral collisions in both p_T intervals and p_T^{jet} selections.

***$R_{D(p_T,r)}$* and charged-particle *p_T*:** In Figure 5, it was shown that for central and mid-central collisions, there is an enhancement of charged particles with $p_T < 4.0$ GeV and a suppression of charged particles with $p_T > 4.0$ GeV. In Figure 7 the p_T dependence for selections in r is directly investigated for 126–158 GeV and 200–251 GeV jets, in the following centrality intervals: 0–10%, 30–40% and 60–80%. Interestingly, there is no significant suppression of the yields in Pb+Pb collisions for $r < 0.05$ at all measured p_T. For larger r values the yields are enhanced for charged particles with $p_T < 4$ GeV and suppressed for

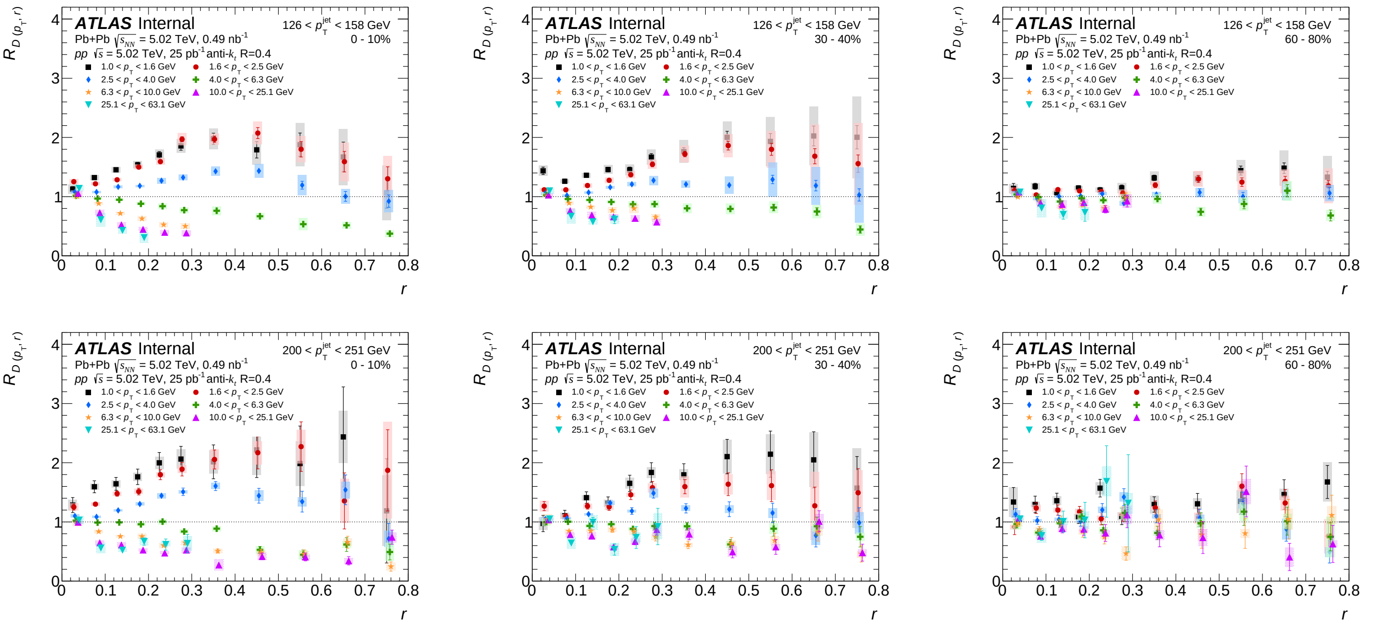

Figure 5: Ratios of $D(p_\mathrm{T}, r)$ distributions in Pb+Pb and pp collisions as a function of angular distance r for $p_\mathrm{T}^\mathrm{jet}$ of 126 to 158 GeV (top) and of 200 to 251 GeV (bottom) for seven p_T selections. Different centrality selections are shown: 0–10% (left), 30–40% (middle), 60–80% (right). The vertical bars on the data points indicate statistical uncertainties while the shaded boxes indicate systematic uncertainties. The widths of the boxes are not indicative of the bin size and the points are shifted horizontally for better visibility.

higher p_T charged particles in both the 0–10% and 30–40% centrality selections and both $p_\mathrm{T}^\mathrm{jet}$ ranges presented here. The magnitude of the enhancement increases for decreasing p_T below 4 GeV while the suppression is enhanced with increasing p_T for 4–10 GeV, after which it is approximately constant. At fixed p_T the magnitude of the deviation from unity is largest for $0.3 < r < 0.4$ and $0.5 < r < 0.6$. In the 60–80% peripheral collisions, the same trend remains true (but with smaller magnitude modifications) for $126 < p_\mathrm{T}^\mathrm{jet} < 158$ GeV; for the higher $p_\mathrm{T}^\mathrm{jet}$ selection the larger uncertainties do not allow a clear conclusion to be drawn for peripheral collisions.

$R_{D(p_\mathrm{T},r)}$ and $p_\mathrm{T}^\mathrm{jet}$: The $R_{D(p_\mathrm{T},r)}$ distributions for low and high p_T particles in the different $p_\mathrm{T}^\mathrm{jet}$ selections are directly overlaid in Figure 8. These distributions are for the 0–10% most central collisions, and show a hint of enhancement in $R_{D(p_\mathrm{T},r)}$ with increasing $p_\mathrm{T}^\mathrm{jet}$ for $r < 0.25$ for low p_T charged particles. No significant $p_\mathrm{T}^\mathrm{jet}$ dependence is seen at larger r values, or for high-p_T charged particles at any r. This $p_\mathrm{T}^\mathrm{jet}$ dependence is further explored by defining an integral over the low p_T excess in Section 7.4.

7.3 $\Delta D(p_\mathrm{T}, r)$ distributions

In addition to the ratios of the $D(p_\mathrm{T}, r)$ distributions, differences between the unfolded charged-particle yields are also evaluated as $\Delta D(p_\mathrm{T}, r)$ to quantify the modification in terms of the particle density. These differences are presented as a function of r for different p_T selections in 0–10% central collisions in Figure 9. These distributions show an excess in the charged-particle yield density for Pb+Pb collisions compared to

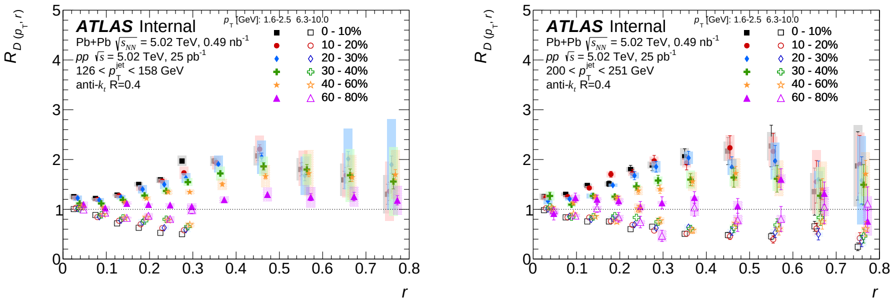

Figure 6: The $R_{D(p_{\mathrm{T}},r)}$ distributions for $p_{\mathrm{T}}^{\mathrm{jet}}$ of 126–158 GeV (left) and 200–251 GeV (right) as a function of angular distance r for two p_{T} selections, 1.6–2.5 GeV (closed symbols) and 6.3–10.0 GeV (open symbols), and six centrality intervals. The vertical bars on the data points indicate statistical uncertainties while the shaded boxes indicate systematic uncertainties. The widths of the boxes are not indicative of the bin size and the points are shifted horizontally for better visibility.

pp collisions for charged particles with $p_{\mathrm{T}} < 4.0$ GeV. This ranges from 0.5 to 4 particles per unit area per GeV for 1 GeV charged particles in 126–158 GeV jets for 0–10% central Pb+Pb collisions and increases with increasing $p_{\mathrm{T}}^{\mathrm{jet}}$. The largest excess for charged particles with $p_{\mathrm{T}} < 4.0$ GeV is within the jet cone. For large r values, the difference decreases, but remains positive. A depletion for higher p_{T} particles of approximately 0.5 particles per unit area per GeV is seen for 126–158 GeV jets in 0–10% central Pb+Pb collisions. The magnitude of this depletion increases for higher $p_{\mathrm{T}}^{\mathrm{jet}}$. There is a minimum in the $\Delta D(p_{\mathrm{T}}, r)$ distributions of charged particles with $4.0 < p_{\mathrm{T}} < 25.1$ GeV at $0.05 < r < 0.10$ that is seen at many $p_{\mathrm{T}}^{\mathrm{jet}}$ ranges under investigation. The magnitudes of the excesses and deficits discussed here are dependent on the selected charged-particle p_{T}.

7.4 p_{T} integrated distributions

Motivated by similar studies of the enhancement of soft fragments in jet fragmentation functions in Pb+Pb compared to *pp* collisions from Ref. [20], the unfolded $D(p_{\mathrm{T}}, r)$ distributions are integrated for charged particles with $p_{\mathrm{T}} < 4$ GeV to construct the quantities $\Theta(r)$ and $P(r)$ defined as:

$$\Theta(r) = \int_{1\,\mathrm{GeV}}^{4\,\mathrm{GeV}} D(p_{\mathrm{T}}, r)\mathrm{d}p_{\mathrm{T}}$$
$$P(r) = \int_{0}^{r} \int_{1\,\mathrm{GeV}}^{4\,\mathrm{GeV}} D(p_{\mathrm{T}}, r')\mathrm{d}p_{\mathrm{T}}\mathrm{d}r'$$

The $\Theta(r)$ values are integrated over the charged-particle p_{T} interval of 1–4 GeV to provide a summary look at the p_{T} region of enhancement discussed above. The $P(r)$ values further add a running integral over r and provide information about the jet shape. Both of these quantities are compared between the *pp* and Pb+Pb systems to give the following distributions:

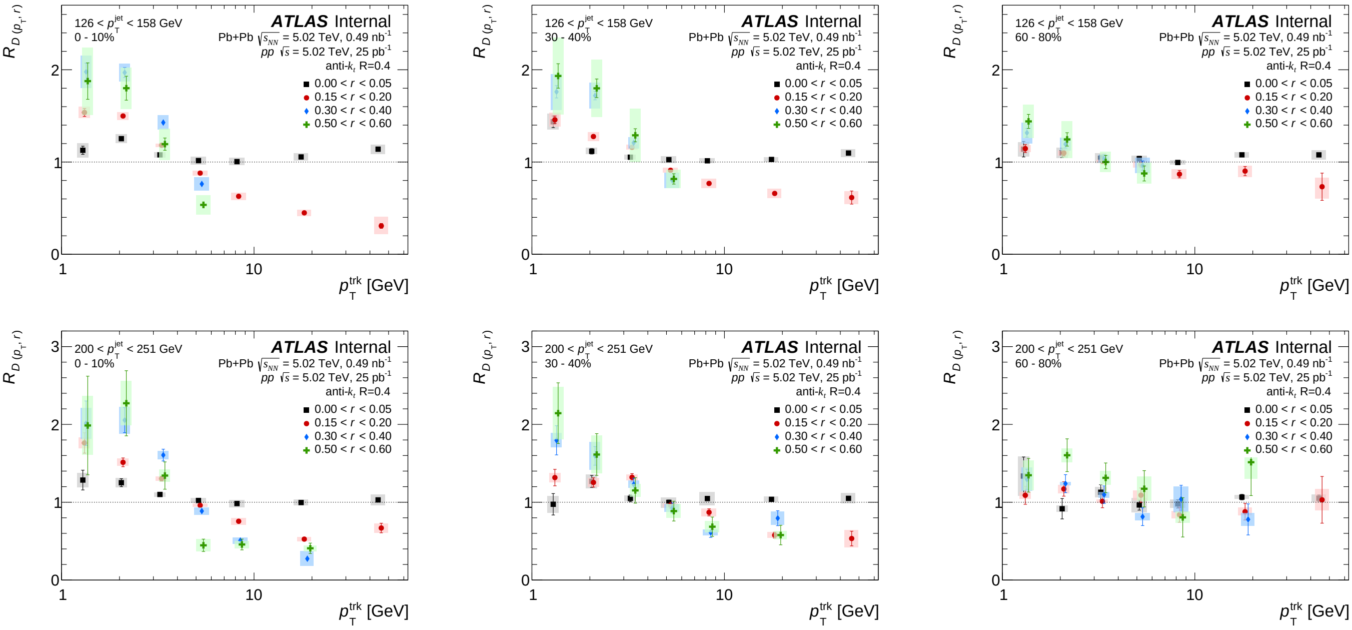

Figure 7: $R_{D(p_{\mathrm{T}},r)}$ as a function of p_{T} for 0–10% (left), 30–40% (middle), and 60–80% (right) Pb+Pb collisions in two different $p_{\mathrm{T}}^{\mathrm{jet}}$ selections: 126–158 GeV (top) and 200–251 GeV (bottom). The different colors indicate different angular distances from the jet axis. The vertical bars on the data points indicate statistical uncertainties while the shaded boxes indicate systematic uncertainties. The widths of the boxes are not indicative of the bin size and the points are shifted horizontally for better visibility.

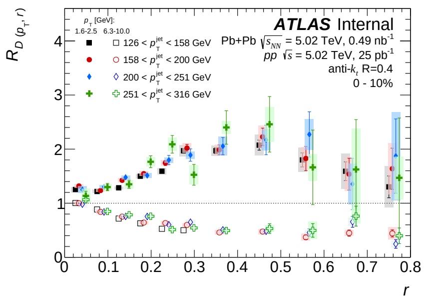

Figure 8: $R_{D(p_{\mathrm{T}},r)}$ as a function of r for 0–10% collisions for charged particles with $1.0 < p_{\mathrm{T}} < 1.6$ GeV (closed symbols) and $6.3 < p_{\mathrm{T}} <10.0$ GeV (open symbols) for different $p_{\mathrm{T}}^{\mathrm{jet}}$ selections. The vertical bars on the data points indicate statistical uncertainties while the shaded boxes indicate systematic uncertainties. The widths of the boxes are not indicative of the bin size and the points are shifted horizontally for better visibility.

$$
\begin{aligned}
\Delta_{\Theta(r)} &= \Theta(r)_{\mathrm{Pb+Pb}} - \Theta(r)_{pp} \\
R_{\Theta(r)} &= \frac{\Theta(r)_{\mathrm{Pb+Pb}}}{\Theta(r)_{\mathrm{pp}}} \\
R_{P(r)} &= \frac{P(r)_{\mathrm{Pb+Pb}}}{P(r)_{pp}}
\end{aligned}
$$

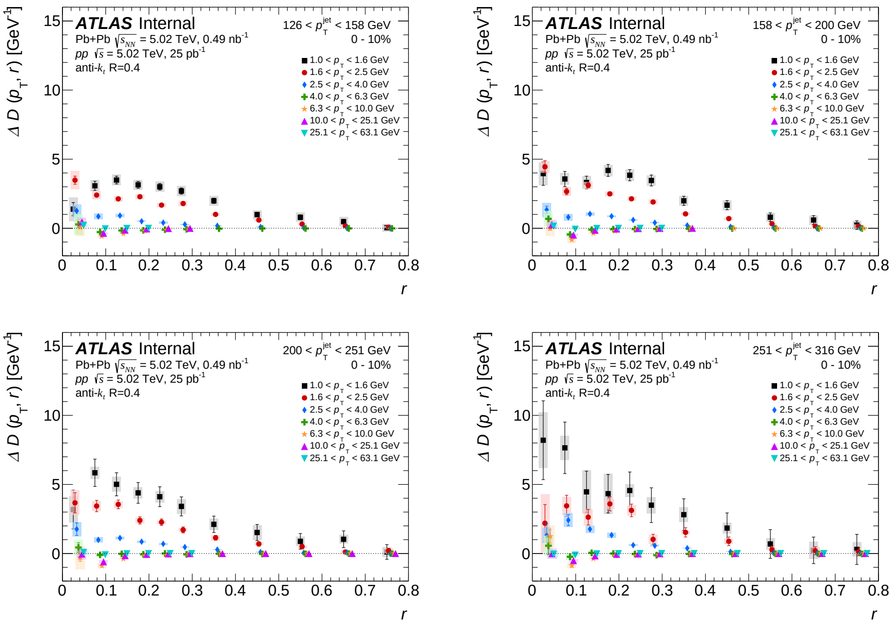

Figure 9: $\Delta D(p_{\mathrm{T}}, r)$ as a function of r in central collisions for all p_{T} ranges in four $p_{\mathrm{T}}^{\mathrm{jet}}$ selections: 126–158 GeV, 158–200 GeV, 200–251 GeV, and 251–316 GeV. The vertical bars on the data points indicate statistical uncertainties while the shaded boxes indicate systematic uncertainties. The widths of the boxes are not indicative of the bin size and the points are shifted horizontally for better visibility.

These aggregate quantities are intended to provide some summary information about the location with respect to the jet axis, magnitude, and $p_{\mathrm{T}}^{\mathrm{jet}}$ dependence of the low-p_{T} charged-particle excess discussed above. The ratio quantities are useful for comparisons to other Pb+Pb measurements; $\Delta_{\Theta(r)}$ is very similar to $\Delta D(p_{\mathrm{T}}, r)$, however it is integrated over charged-particle p_{T} in the 1–4 GeV interval.

Figure 10 shows the $\Delta_{\Theta(r)}$ distributions as a function of r in centrality intervals: 0–10%, 30–40%, 60–80%. In the most central collisions, a significant $p_{\mathrm{T}}^{\mathrm{jet}}$ dependence to $\Delta_{\Theta(r)}$ is observed; for $r < 0.4$ (particles within the jet cone) $\Delta_{\Theta(r)}$ increases with increasing $p_{\mathrm{T}}^{\mathrm{jet}}$. The value of $\Delta_{\Theta(r)}$ decreases in more peripheral collisions and the $p_{\mathrm{T}}^{\mathrm{jet}}$ dependence is no longer significant.

Figure 11 shows $R_{\Theta(r)}$ and $R_{P(r)}$ for the following centrality intervals: 0–10%, 30–40% and 60–80%. The $R_{\Theta(r)}$ distributions of the most central collisions show a maximum for $r \sim 0.4$ and a flattening or a decrease for larger r. However, since $R_{\Theta(r)}$ remains at or above unity for the full range of r values presented $R_{P(r)}$ continues to slowly increase with increasing r over the full measured range. In more peripheral collisions, the magnitude of the excess is reduced and the trends in $R_{\Theta(r)}$ are less clear, however the slow increase of $R_{P(r)}$ is clearly seen for the 30–40% central collisions. The flattening of the $R_{P(r)}$ distributions demonstrates what while wider jets have a softer fragmentation and contain more particles with less p_{T} in Pb+Pb compared to pp collisions [60, 61], this effect does not extend to arbitrarily large distances and flattens out for jets with radius larger than 0.6.

Calculations done in Ref. [30] show that the response of the QGP medium to the jet has a non-trivial contribution to the modification of the jet properties between pp and Pb+Pb even up to $r = 1.0$ from the jet axis. The plateauing and slight decrease seen in Figure 5 for the $R_{D(p_{\mathrm{T}},r)}$ distributions in central Pb+Pb

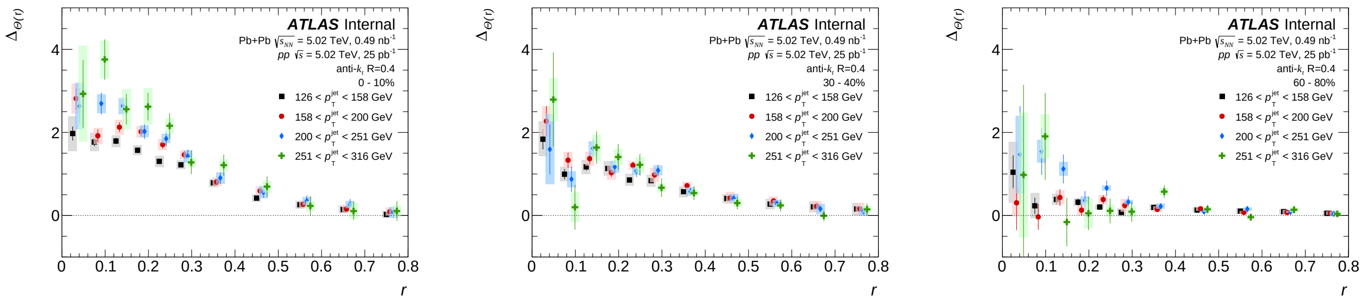

Figure 10: $\Delta_{\Theta(r)}$ as a function of r for charged particles with p_T < 4 GeV in four p_T^{jet} selections: 126–158 GeV, 158–200 GeV, 200–251 GeV, and 251–316 GeVand three centrality selections: 0–10% (left), 30–40% (middle) and 60–80% (right). The vertical bars on the data points indicate statistical uncertainties while the shaded boxes indicate systematic uncertainties. The widths of the boxes are not indicative of the bin size and the points are shifted horizontally for better visibility.

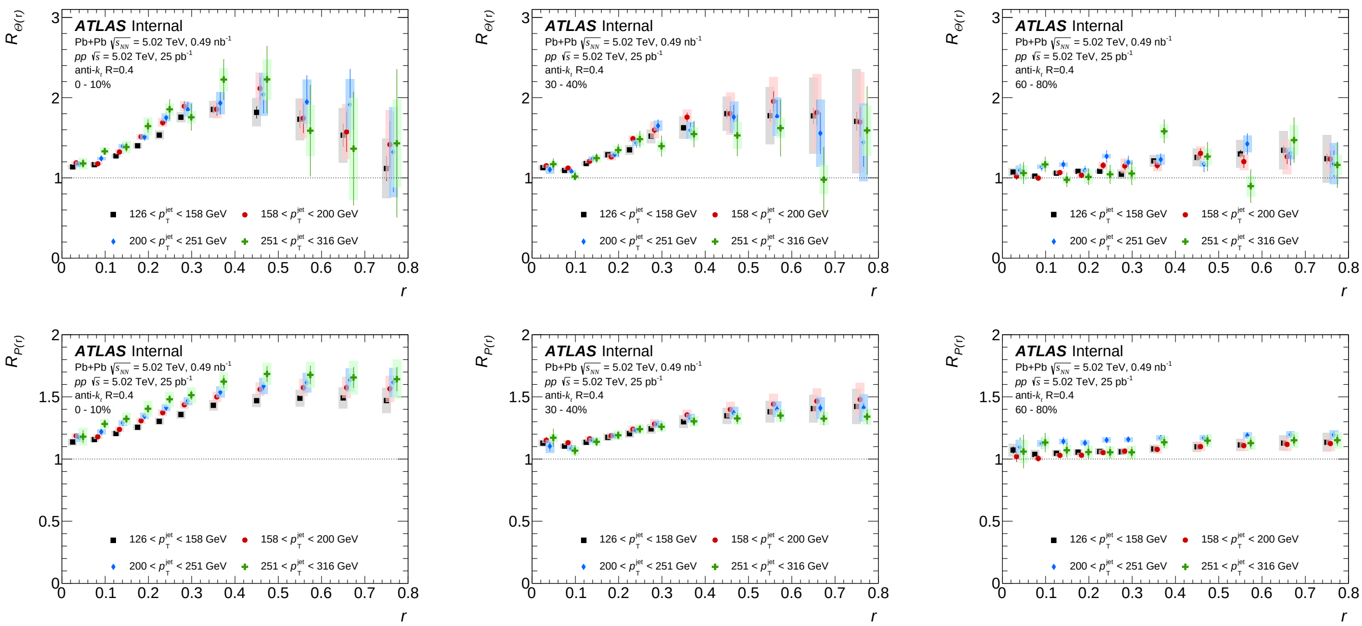

Figure 11: $R_{\Theta(r)}$ (top) and $R_{P(r)}$ (bottom) as a function of r for charged particles with p_T < 4 GeV ranges in four p_T^{jet} selections: 126–158 GeV, 158–200 GeV, 200–251 GeV, and 251–316 GeV and three centrality selections: 0–10% (left), 30–40% (middle) and 60–80% (rights). The vertical bars on the data points indicate statistical uncertainties while the shaded boxes indicate systematic uncertainties. The widths of the boxes are not indicative of the bin size and the points are shifted horizontally for better visibility.

collisions beyond $r = 0.6$ from the jet axis suggests that perhaps the response of the QGP to the jet is not as large for $r > 0.6$, and that the QGP is unaffected by the presence of the jet in this region

There are two possible explanations of the enhancement of charged particles in the kinematic region of $p_{\mathrm{T}} < 4$ GeV. First, gluon radiation from the hard scattered parton as it propagates through the QGP would lead to extra soft particles [62, 63]. Second, the interactions of a jet with the QGP and its hydrodynamic response could induce a wake that manifests itself as an enhancement of low p_{T} particles [30].

The observed modification at $p_{\mathrm{T}} > 4$ GeV can be explained on the basis of the larger expected energy loss of gluon-initiated jets, resulting in a relative enhancement of quark jets in Pb+Pb collisions compared to pp collisions at a given $p_{\mathrm{T}}^{\mathrm{jet}}$ value [20, 64]. Since gluon jets have a broader distribution of particle transverse momentum with respect to the jet direction compared to quark-initiated jets [65], such an effect could describe the narrowing of the particle distribution around the jet direction for particles with $p_{\mathrm{T}} > 4.0$ GeV that is observed here, though no calculations of this are available.

8 Summary

This paper presents a measurement of the yields of charged particles, $D(p_{\mathrm{T}}, r)$, inside and around $R = 0.4$ anti-k_t jets with $|y^{\mathrm{jet}}| < 1.7$ up to a distance of $r = 0.8$ from the jet axis. The yields are measured in intervals of $p_{\mathrm{T}}^{\mathrm{jet}}$ from 126 to 316 GeV in Pb+Pb and pp collisions at 5.02 TeV as a function of charged-particle p_{T} and the angular distance r between the jet axis and charged particle.

These results show a broadening of the $D(p_{\mathrm{T}}, r)$ distribution for low p_{T} particles inside the jet in central Pb+Pb collisions compared to those in pp collisions while for higher p_{T} particles angular distributions are narrower in Pb+Pb collisions compared to pp collisions. These modifications are centrality dependent and decrease for more peripheral collisions. The $R_{D(p_{\mathrm{T}},r)}$ distributions for charged particles with $p_{\mathrm{T}} < 4$ GeV are above unity and grow with increasing angular separation up to $r \sim 0.3$, showing weak to no dependence on r in the interval $0.3 < r < 0.6$ followed with a small decrease in the enhancement for $0.6 < r < 0.8$. For charged particles with $p_{\mathrm{T}} > 4$ GeV, a suppression in $R_{D(p_{\mathrm{T}},r)}$ is observed, and the distributions decrease with increasing r for $0.05 < r < 0.3$, with no r dependence for $r > 0.3$. For all charged-particle p_{T} values, the $R_{D(p_{\mathrm{T}},r)}$ values are greater than or equal to unity for $r < 0.05$. Between $0.1 < r < 0.25$, a statistically significant trend of increasing $R_{D(p_{\mathrm{T}},r)}$ with increasing $p_{\mathrm{T}}^{\mathrm{jet}}$ is observed for low-p_{T} particles. No significant $p_{\mathrm{T}}^{\mathrm{jet}}$ dependence is seen for particles with $p_{\mathrm{T}} > 4$ GeV.

This measurement provides information about the modification of the jet at large distances from the jet axis that can be used to constrain models that distinguish the modifications of jet due to the presence of the plasma from the response of the medium to the jet.

Acknowledgements

We thank CERN for the very successful operation of the LHC, as well as the support staff from our institutions without whom ATLAS could not be operated efficiently.

We acknowledge the support of ANPCyT, Argentina; YerPhI, Armenia; ARC, Australia; BMWFW and FWF, Austria; ANAS, Azerbaijan; SSTC, Belarus; CNPq and FAPESP, Brazil; NSERC, NRC and CFI, Canada; CERN; CONICYT, Chile; CAS, MOST and NSFC, China; COLCIENCIAS, Colombia;

MSMT CR, MPO CR and VSC CR, Czech Republic; DNRF and DNSRC, Denmark; IN2P3-CNRS, CEA-DRF/IRFU, France; SRNSFG, Georgia; BMBF, HGF, and MPG, Germany; GSRT, Greece; RGC, Hong Kong SAR, China; ISF and Benoziyo Center, Israel; INFN, Italy; MEXT and JSPS, Japan; CNRST, Morocco; NWO, Netherlands; RCN, Norway; MNiSW and NCN, Poland; FCT, Portugal; MNE/IFA, Romania; MES of Russia and NRC KI, Russian Federation; JINR; MESTD, Serbia; MSSR, Slovakia; ARRS and MIZŠ, Slovenia; DST/NRF, South Africa; MINECO, Spain; SRC and Wallenberg Foundation, Sweden; SERI, SNSF and Cantons of Bern and Geneva, Switzerland; MOST, Taiwan; TAEK, Turkey; STFC, United Kingdom; DOE and NSF, United States of America. In addition, individual groups and members have received support from BCKDF, CANARIE, CRC and Compute Canada, Canada; COST, ERC, ERDF, Horizon 2020, and Marie Skłodowska-Curie Actions, European Union; Investissements d' Avenir Labex and Idex, ANR, France; DFG and AvH Foundation, Germany; Herakleitos, Thales and Aristeia programmes co-financed by EU-ESF and the Greek NSRF, Greece; BSF-NSF and GIF, Israel; CERCA Programme Generalitat de Catalunya, Spain; The Royal Society and Leverhulme Trust, United Kingdom.

The crucial computing support from all WLCG partners is acknowledged gratefully, in particular from CERN, the ATLAS Tier-1 facilities at TRIUMF (Canada), NDGF (Denmark, Norway, Sweden), CC-IN2P3 (France), KIT/GridKA (Germany), INFN-CNAF (Italy), NL-T1 (Netherlands), PIC (Spain), ASGC (Taiwan), RAL (UK) and BNL (USA), the Tier-2 facilities worldwide and large non-WLCG resource providers. Major contributors of computing resources are listed in Ref. [66].

References

[1] G. Roland, K. Šafařík and P. Steinberg, *Heavy-ion collisions at the LHC*, Prog. Part. Nucl. Phys. **77** (2014) 70 (cit. on p. 2).

[2] W. Busza, K. Rajagopal and W. van der Schee, *Heavy Ion Collisions: The Big Picture, and the Big Questions*, Ann. Rev. Nucl. Part. Sci. **68** (2018) 339, arXiv: `1802.04801 [hep-ph]` (cit. on p. 2).

[3] ALICE Collaboration, *Measurement of charged jet suppression in Pb-Pb collisions at $\sqrt{s_{NN}} = 2.76$ TeV*, JHEP **03** (2014) 013, arXiv: `1311.0633 [nucl-ex]` (cit. on p. 2).

[4] ATLAS Collaboration, *Measurements of the Nuclear Modification Factor for Jets in Pb+Pb Collisions at $\sqrt{s_{\mathrm{NN}}} = 2.76$ TeV with the ATLAS Detector*, Phys. Rev. Lett. **114** (2015) 072302, arXiv: `1411.2357 [hep-ex]` (cit. on p. 2).

[5] ALICE Collaboration, *Measurement of jet suppression in central Pb-Pb collisions at $\sqrt{s_{\mathrm{NN}}} = 2.76$ TeV*, Phys. Lett. B **746** (2015) 1, arXiv: `1502.01689 [nucl-ex]` (cit. on p. 2).

[6] CMS Collaboration, *Measurement of inclusive jet cross sections in pp and PbPb collisions at $\sqrt{s_{NN}} = 2.76$ TeV*, Phys. Rev. C **96** (2017) 015202, arXiv: `1609.05383 [nucl-ex]` (cit. on p. 2).

[7] ATLAS Collaboration, *Measurement of the nuclear modification factor for inclusive jets in Pb+Pb collisions at $\sqrt{s_{\mathrm{NN}}} = 5.02$ TeV with the ATLAS detector*, Phys. Lett. B **790** (2019) 108, arXiv: `1805.05635 [nucl-ex]` (cit. on pp. 2, 4).

[8] ATLAS Collaboration, *Observation of a Centrality-Dependent Dijet Asymmetry in Lead-Lead Collisions at $\sqrt{s_{NN}} = 2.76$ TeV with the ATLAS Detector at the LHC*, Phys. Rev. Lett. **105** (2010) 252303, arXiv: `1011.6182 [hep-ex]` (cit. on p. 2).

[9] CMS Collaboration, *Observation and studies of jet quenching in PbPb collisions at $\sqrt{s_{NN}} = 2.76$ TeV*, Phys. Rev. C **84** (2011) 024906, arXiv: 1102.1957 [nucl-ex] (cit. on p. 2).

[10] ATLAS Collaboration, *Measurement of jet p_{T} correlations in Pb+Pb and pp collisions at $\sqrt{s_{\mathrm{NN}}} = 2.76$ TeV with the ATLAS detector*, Phys. Lett. B **774** (2017) 379, arXiv: 1706.09363 [hep-ex] (cit. on pp. 2, 11).

[11] CMS Collaboration, *Studies of jet quenching using isolated-photon+jet correlations in PbPb and pp collisions at $\sqrt{s_{NN}} = 2.76$ TeV*, Phys. Lett. B **718** (2013) 773, arXiv: 1205.0206 [nucl-ex] (cit. on p. 2).

[12] ATLAS Collaboration, *Measurement of photon–jet transverse momentum correlations in 5.02 TeV Pb+Pb and pp collisions with ATLAS*, Phys. Lett. B **789** (2019) 167, arXiv: 1809.07280 [nucl-ex] (cit. on p. 2).

[13] ATLAS Collaboration, *Measurement of the jet fragmentation function and transverse profile in proton-proton collisions at a center-of-mass energy of 7 TeV with the ATLAS detector*, Eur. Phys. J. C **71** (2011) 1795, arXiv: 1109.5816 [hep-ex] (cit. on p. 2).

[14] ALICE Collaboration, *Medium modification of the shape of small-radius jets in central Pb-Pb collisions at $\sqrt{s_{\mathrm{NN}}} = 2.76$ TeV*, JHEP **10** (2018) 139, arXiv: 1807.06854 [nucl-ex] (cit. on p. 2).

[15] CMS Collaboration, *Shape, transverse size, and charged-hadron multiplicity of jets in pp collisions at $\sqrt{s} = 7$ TeV*, JHEP **06** (2012) 160, arXiv: 1204.3170 [hep-ex] (cit. on p. 2).

[16] CMS Collaboration, *Modification of jet shapes in PbPb collisions at $\sqrt{s_{\mathrm{NN}}} = 2.76$ TeV*, Phys. Lett. B **730** (2014) 243, arXiv: 1310.0878 [nucl-ex] (cit. on p. 2).

[17] ATLAS Collaboration, *Measurement of inclusive jet charged-particle fragmentation functions in Pb+Pb collisions at $\sqrt{s_{NN}} = 2.76$ TeV with the ATLAS detector*, Phys. Lett. B **739** (2014) 320, arXiv: 1406.2979 [hep-ex] (cit. on p. 2).

[18] CMS Collaboration, *Measurement of jet fragmentation in PbPb and pp collisions at $\sqrt{s_{NN}} = 2.76$ TeV*, Phys. Rev. C **90** (2014) 024908, arXiv: 1406.0932 [nucl-ex] (cit. on p. 2).

[19] ATLAS Collaboration, *Measurement of jet fragmentation in Pb+Pb and pp collisions at $\sqrt{s_{\mathrm{NN}}} = 2.76$ TeV with the ATLAS detector at the LHC*, Eur. Phys. J. C **77** (2017) 379, arXiv: 1702.00674 [hep-ex] (cit. on pp. 2, 5, 9, 11).

[20] ATLAS Collaboration, *Measurement of jet fragmentation in Pb+Pb and pp collisions at $\sqrt{s_{NN}} = 5.02$ TeV with the ATLAS detector*, Phys. Rev. C **98** (2018) 024908, arXiv: 1805.05424 [nucl-ex] (cit. on pp. 2, 3, 6, 9, 11, 14, 18).

[21] CMS Collaboration, *Measurement of transverse momentum relative to dijet systems in PbPb and pp collisions at $\sqrt{s_{\mathrm{NN}}} = 2.76$ TeV*, JHEP **01** (2016) 006, arXiv: 1509.09029 [nucl-ex] (cit. on p. 2).

[22] CMS Collaboration, *Decomposing transverse momentum balance contributions for quenched jets in PbPb collisions at $\sqrt{s_{\mathrm{NN}}} = 2.76$ TeV*, JHEP **11** (2016) 055, arXiv: 1609.02466 [nucl-ex] (cit. on p. 2).

[23] CMS Collaboration, *Jet properties in PbPb and pp collisions at $\sqrt{s_{\mathrm{NN}}} = 5.02$ TeV*, JHEP **05** (2018) 006, arXiv: 1803.00042 [nucl-ex] (cit. on p. 2).

[24] I. Vitev, S. Wicks and B.-W. Zhang, *A theory of jet shapes and cross sections: from hadrons to nuclei*, JHEP **11** (2008) 093, arXiv: 0810.2807 [hep-ph] (cit. on p. 2).

[25] G. Ovanesyan and I. Vitev, *An effective theory for jet propagation in dense QCD matter: jet broadening and medium-induced bremsstrahlung*, JHEP **06** (2011) 080, arXiv: 1103.1074 [hep-ph] (cit. on p. 2).

[26] J.-P. Blaizot, Y. Mehtar-Tani and M. A. C. Torres, *Angular Structure of the In-Medium QCD Cascade*, Phys. Rev. Lett. **114** (2015) 222002, arXiv: 1407.0326 [hep-ph] (cit. on p. 2).

[27] G.-Y. Qin and X.-N. Wang, *Jet quenching in high-energy heavy-ion collisions*, Int. J. Mod. Phys. E **24** (2015) 1530014, arXiv: 1511.00790 [hep-ph] (cit. on p. 2).

[28] M. A. Escobedo and E. Iancu, *Event-by-event fluctuations in the medium-induced jet evolution*, JHEP **05** (2016) 008, arXiv: 1601.03629 [hep-ph] (cit. on p. 2).

[29] J. Casalderrey-Solana, D. Gulhan, G. Milhano, D. Pablos and K. Rajagopal, *Angular structure of jet quenching within a hybrid strong/weak coupling model*, JHEP **03** (2017) 135, arXiv: 1609.05842 [hep-ph] (cit. on p. 2).

[30] Y. Tachibana, N.-B. Chang and G.-Y. Qin, *Full jet in quark-gluon plasma with hydrodynamic medium response*, Phys. Rev. C **95** (2017) 044909, arXiv: 1701.07951 [nucl-th] (cit. on pp. 2, 16, 18).

[31] ATLAS Collaboration, *The ATLAS Experiment at the CERN Large Hadron Collider*, JINST **3** (2008) S08003 (cit. on p. 3).

[32] ATLAS Collaboration, *ATLAS Insertable B-Layer Technical Design Report*, (2010), ATLAS-TDR-19, URL: http://cds.cern.ch/record/1291633 (cit. on p. 3).

[33] ATLAS Collaboration, *ATLAS Insertable B-Layer Technical Design Report Addendum*, (2012), ATLAS-TDR-19-ADD-1, URL: http://cds.cern.ch/record/1451888 (cit. on p. 3).

[34] ATLAS Collaboration, *Performance of the ATLAS trigger system in 2015*, Eur. Phys. J. C **77** (2017) 317, arXiv: 1611.09661 [hep-ex] (cit. on p. 3).

[35] ATLAS Collaboration, *Measurement of jet fragmentation in 5.02 TeV proton-lead and proton-proton collisions with the ATLAS detector*, Nucl. Phys. A **978** (2018) 65, arXiv: 1706.02859 [hep-ex] (cit. on pp. 4, 6).

[36] P. Nason, *A new method for combining NLO QCD with shower Monte Carlo algorithms*, JHEP **11** (2004) 040, arXiv: hep-ph/0409146 [hep-ph] (cit. on p. 4).

[37] T. Sjöstrand et al., *An introduction to PYTHIA 8.2*, Comput. Phys. Commun. **191** (2015) 159, arXiv: 1410.3012 [hep-ph] (cit. on p. 4).

[38] ATLAS Collaboration, *ATLAS Pythia 8 tunes to 7 TeV data*, ATL-PHYS-PUB-2014-021, 2014, URL: https://cds.cern.ch/record/1966419 (cit. on p. 4).

[39] R. D. Ball et al., *Parton distributions with LHC data*, Nucl. Phys. B **867** (2013) 244, arXiv: 1207.1303 [hep-ph] (cit. on p. 4).

[40] ATLAS Collaboration, *Measurement of longitudinal flow decorrelations in Pb+Pb collisions at $\sqrt{s_{\mathrm{NN}}} = 2.76$ and 5.02 TeV with the ATLAS detector*, Eur. Phys. J. C **78** (2018) 142, arXiv: 1709.02301 [nucl-ex] (cit. on p. 4).

[41] X.-N. Wang and M. Gyulassy, *HIJING: A Monte Carlo model for multiple jet production in* pp, pA, *and* AA *collisions*, Phys. Rev. D **44** (1991) 3501 (cit. on p. 4).

[42] S. Agostinelli et al., *Geant4—a simulation toolkit*, Nucl. Instrum. Meth. A **506** (2003) 250 (cit. on p. 4).

[43] ATLAS Collaboration, *The ATLAS Simulation Infrastructure*, Eur. Phys. J. C **70** (2010) 823, arXiv: 1005.4568 [physics.ins-det] (cit. on pp. 4, 5).

[44] M. Cacciari, G. P. Salam and G. Soyez, *The Anti-k_t jet clustering algorithm*, JHEP **0804** (2008) 063, arXiv: 0802.1189 [hep-ph] (cit. on p. 4).

[45] M. Cacciari, G. P. Salam and G. Soyez, *FastJet User Manual*, Eur. Phys. J. C **72** (2012) 1896, arXiv: 1111.6097 [hep-ph] (cit. on p. 4).

[46] ATLAS Collaboration, *Measurement of the azimuthal anisotropy for charged particle production in $\sqrt{s_{NN}} = 2.76$ TeV lead-lead collisions with the ATLAS detector*, Phys. Rev. C **86** (2012) 014907, arXiv: 1203.3087 [hep-ex] (cit. on pp. 5, 6).

[47] ATLAS Collaboration, *Jet energy scale measurements and their systematic uncertainties in proton-proton collisions at $\sqrt{s} = 13$ TeV with the ATLAS detector*, Phys. Rev. D **96** (2017) 072002, arXiv: 1703.09665 [hep-ex] (cit. on pp. 5, 8).

[48] ATLAS Collaboration, *Properties of jets and inputs to jet reconstruction and calibration with the ATLAS detector using proton–proton collisions at $\sqrt{s} = 13$ TeV*, ATL-PHYS-PUB-2015-036, 2015, URL: https://cds.cern.ch/record/2044564 (cit. on p. 5).

[49] ATLAS Collaboration, *Measurement of photon-jet transverse momentum correlations in 5.02 TeV Pb+Pb and pp collisions with ATLAS*, Phys. Lett. B **789** (2019) 167, arXiv: 1809.07280 [nucl-ex] (cit. on p. 5).

[50] ATLAS Collaboration, *Performance of the ATLAS track reconstruction algorithms in dense environments in LHC Run 2*, Eur. Phys. J. C **77** (2017) 673, arXiv: 1704.07983 [hep-ex] (cit. on p. 5).

[51] G. D'Agostini, *A multidimensional unfolding method based on Bayes' theorem*, Nucl. Instrum. Meth. A **362** (1995) 487 (cit. on p. 6).

[52] T. Adye, *Unfolding algorithms and tests using RooUnfold*, Proceedings of the PHYSTAT 2011 Workshop, CERN-2011-006 (2011), arXiv: 1105.1160 [physics.data-an] (cit. on p. 6).

[53] ATLAS Collaboration, *Jet energy measurement with the ATLAS detector in proton-proton collisions at $\sqrt{s} = 7$ TeV*, Eur. Phys. J. C **73** (2013) 2304, arXiv: 1112.6426 [hep-ex] (cit. on pp. 6, 8).

[54] ATLAS Collaboration, *Jet energy scale and its uncertainty for jets reconstructed using the ATLAS heavy ion jet algorithm*, ATLAS-CONF-2015-016, 2015, URL: http://cds.cern.ch/record/2008677 (cit. on p. 8).

[55] ATLAS Collaboration, *Jet energy measurement and its systematic uncertainty in proton-proton collisions at $\sqrt{s} = 7$ TeV with the ATLAS detector*, Eur. Phys. J. C **75** (2015) 17, arXiv: 1406.0076 [hep-ex] (cit. on p. 8).

[56] ATLAS Collaboration, *Jet energy resolution in proton-proton collisions at $\sqrt{s} = 7$ TeV recorded in 2010 with the ATLAS detector*, Eur. Phys. J. C **73** (2013) 2306, arXiv: 1210.6210 [hep-ex] (cit. on p. 8).

[57] ATLAS Collaboration, *Data-driven determination of the energy scale and resolution of jets reconstructed in the ATLAS calorimeters using dijet and multijet events at $\sqrt{s} = 8$ TeV*, (2015), ATLAS-CONF-2015-017, URL: https://cds.cern.ch/record/2008678 (cit. on p. 8).

[58] ATLAS Collaboration, *Early Inner Detector Tracking Performance in the 2015 Data at $\sqrt{s} = 13$ TeV*, ATL-PHYS-PUB-2015-051, 2015, URL: https://cds.cern.ch/record/2110140 (cit. on p. 9).

[59] ATLAS Collaboration, *Measurement of track reconstruction inefficiencies in the core of jets via pixel dE/dx with the ATLAS experiment using $\sqrt{s} = 13$ TeV pp collision data*, ATL-PHYS-PUB-2016-007, 2016, URL: https://cds.cern.ch/record/2140460 (cit. on p. 9).

[60] P. M. Chesler and K. Rajagopal, *On the evolution of jet energy and opening angle in strongly coupled plasma*, JHEP **2016** (2016) 98, ISSN: 1029-8479, URL: https://doi.org/10.1007/JHEP05(2016)098 (cit. on p. 16).

[61] Z. Hulcher, D. Pablos and K. Rajagopal, *Resolution Effects in the Hybrid Strong/Weak Coupling Model*, (2017), arXiv: 1707.05245 [hep-ph] (cit. on p. 16).

[62] Y.-T. Chien, A. Emerman, Z.-B. Kang, G. Ovanesyan and I. Vitev, *Jet Quenching from QCD Evolution*, Phys. Rev. D **93** (2016) 074030, arXiv: 1509.02936 [hep-ph] (cit. on p. 18).

[63] Z.-B. Kang, F. Ringer and I. Vitev, *Inclusive production of small radius jets in heavy-ion collisions*, Phys. Lett. B **769** (2017) 242, arXiv: 1701.05839 [hep-ph] (cit. on p. 18).

[64] M. Spousta and B. Cole, *Interpreting single jet measurements in Pb+Pb collisions at the LHC*, Eur. Phys. J. C **76** (2016) 50, arXiv: 1504.05169 [hep-ph] (cit. on p. 18).

[65] OPAL Collaboration, *A Model independent measurement of quark and gluon jet properties and differences*, Z. Phys. C **68** (1995) 179 (cit. on p. 18).

[66] ATLAS Collaboration, *ATLAS Computing Acknowledgements*, ATL-GEN-PUB-2016-002, URL: https://cds.cern.ch/record/2202407 (cit. on p. 19).

Auxiliary material

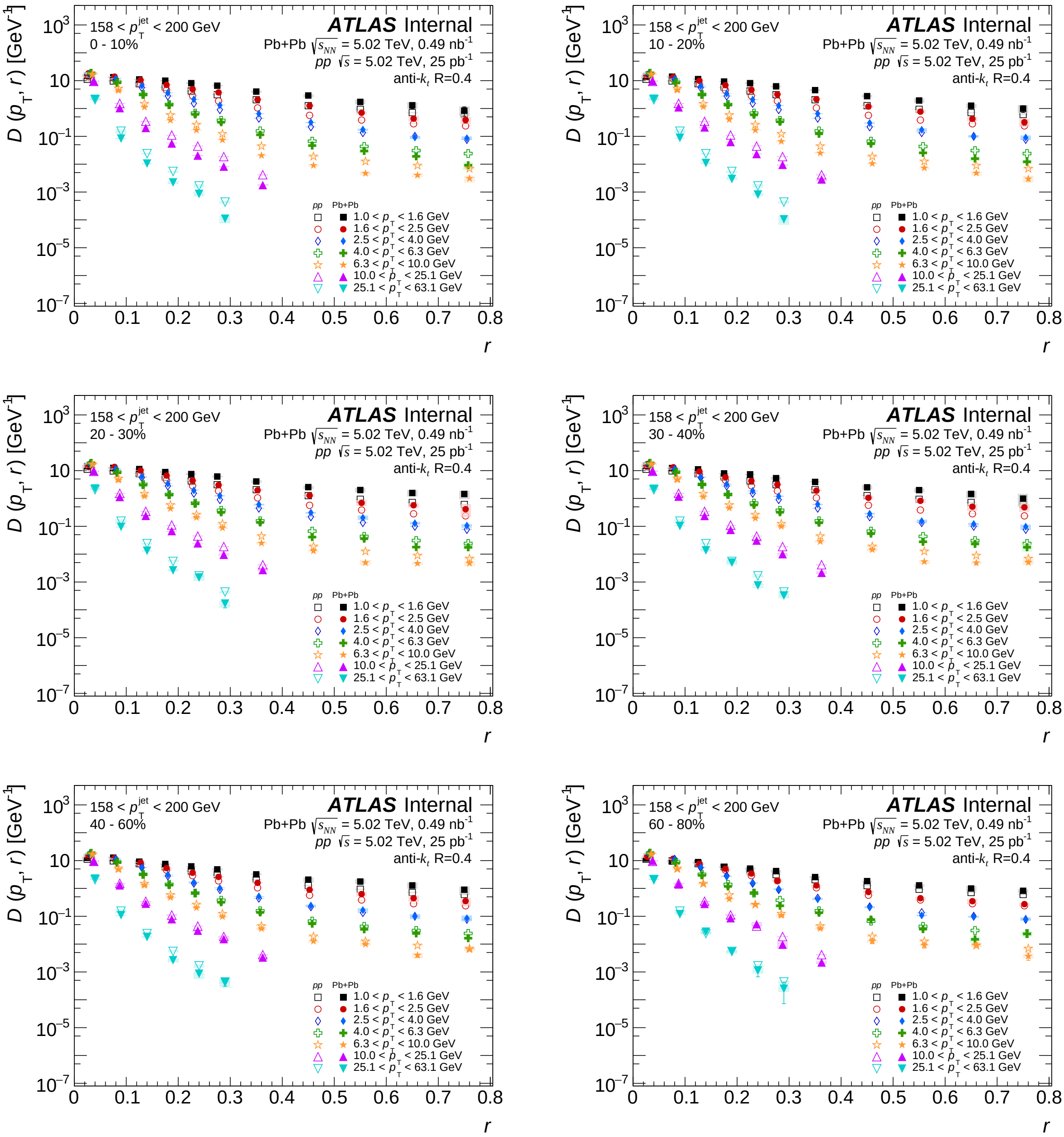

Figure 12: $D(p_{\mathrm{T}}, r)$ distributions as a function of r for different p_{T} ranges in 158–200 GeV jets. The open markers are for pp collisions and the solid markers are for Pb+Pb collisions. The different panels refer to different centrality selections. The vertical bars on the data points indicate statistical uncertainties while the shaded boxes indicate systematic uncertainties. The widths of the boxes are not indicative of the bin size and the points are shifted horizontally for better visibility. The distributions for $p_{\mathrm{T}} > 6.3$ GeV are restricted to smaller r values as discussed in Section 5.

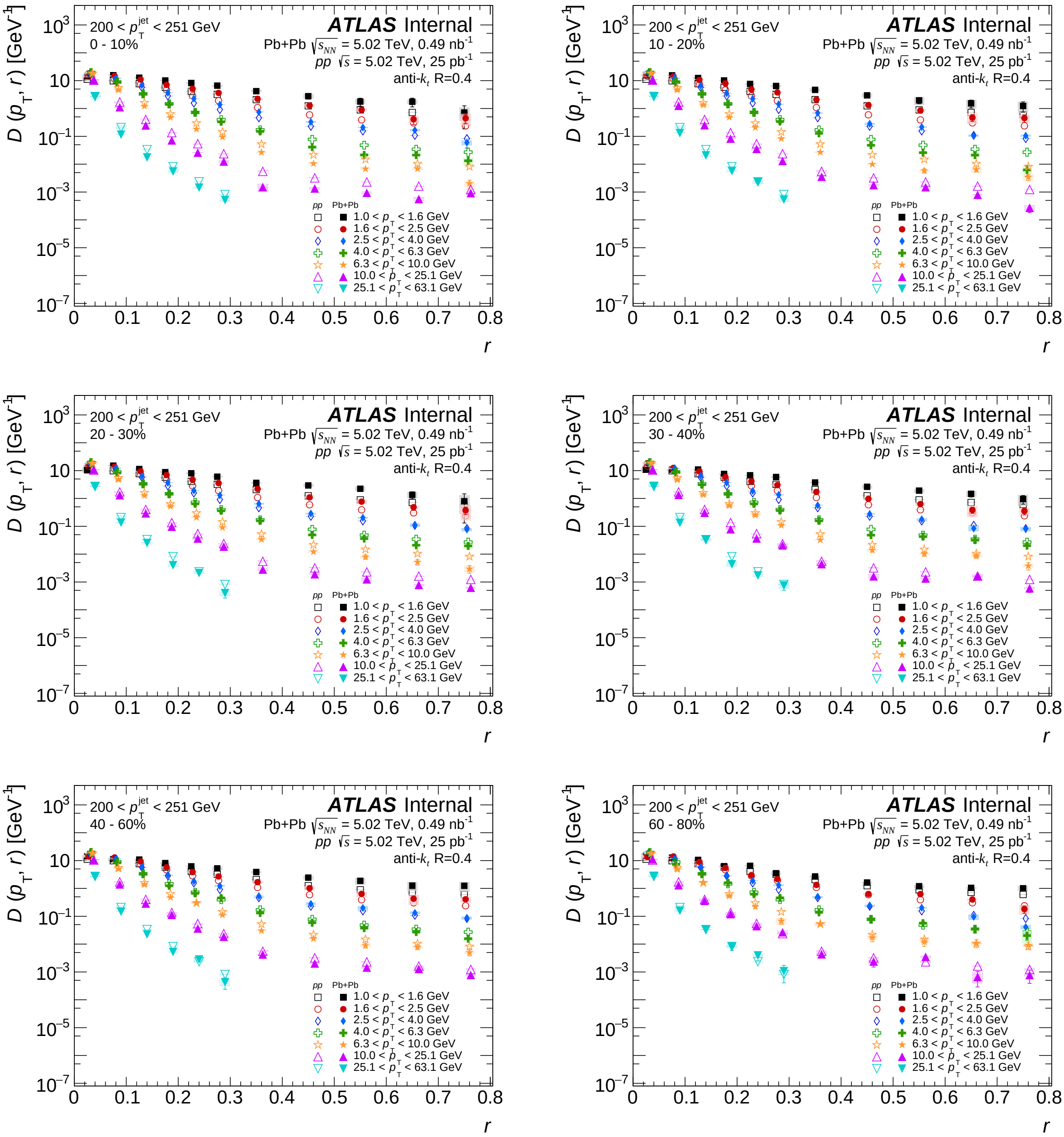

Figure 13: $D(p_{\mathrm{T}}, r)$ distributions as a function of r for different p_{T} ranges in 200–251 GeV jets. The open markers are for pp collisions and the solid markers are for Pb+Pb collisions. The different panels refer to different centrality selections. The vertical bars on the data points indicate statistical uncertainties while the shaded boxes indicate systematic uncertainties. The widths of the boxes are not indicative of the bin size and the points are shifted horizontally for better visibility. The distributions for $p_{\mathrm{T}} > 6.3$ GeV are restricted to smaller r values as discussed in Section 5.

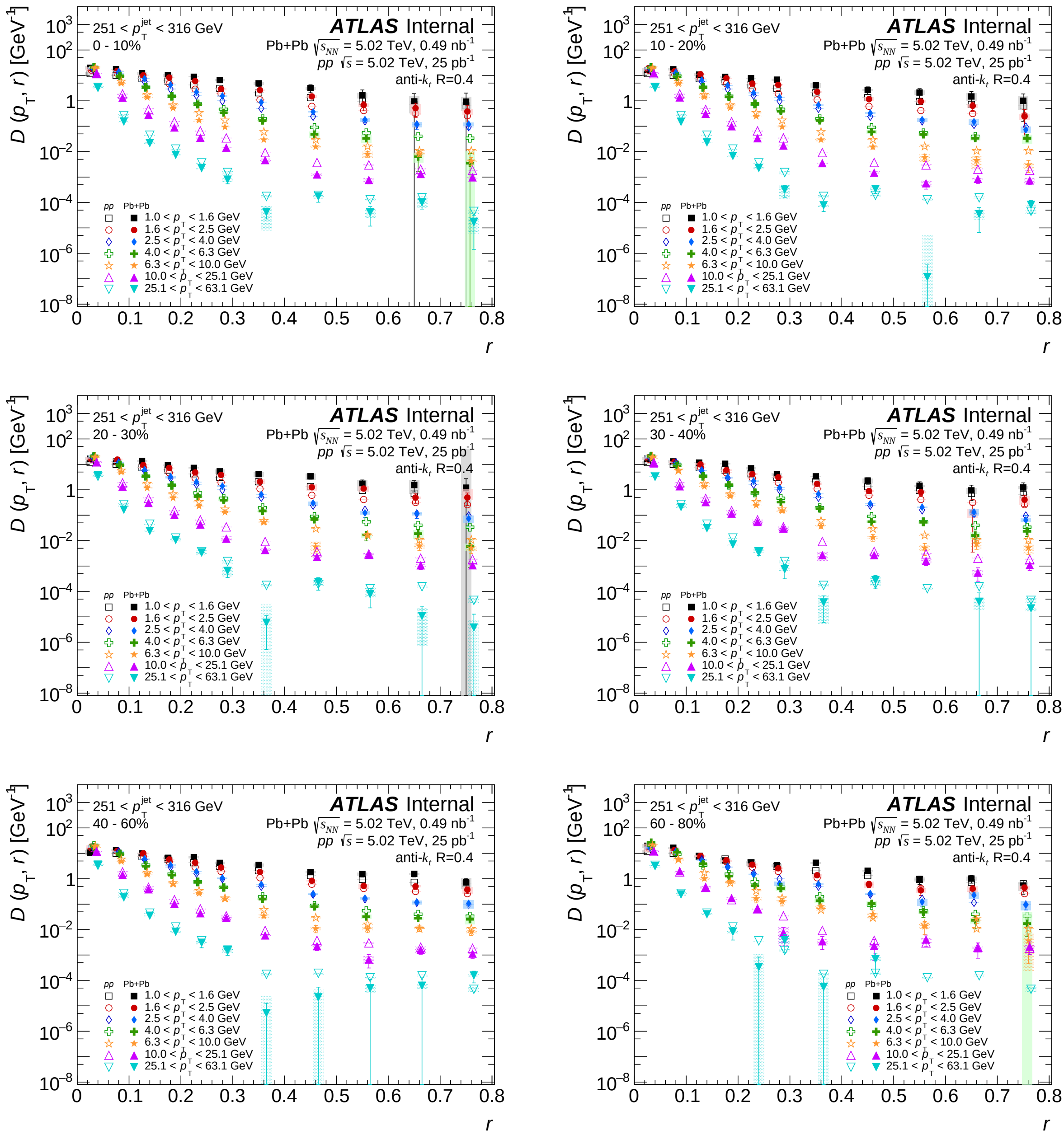

Figure 14: $D(p_{\mathrm{T}}, r)$ distributions as a function of r for different p_{T} ranges in 251–316 GeV jets. The open markers are for pp collisions and the solid markers are for Pb+Pb collisions. The different panels refer to different centrality selections. The vertical bars on the data points indicate statistical uncertainties while the shaded boxes indicate systematic uncertainties. The widths of the boxes are not indicative of the bin size and the points are shifted horizontally for better visibility.

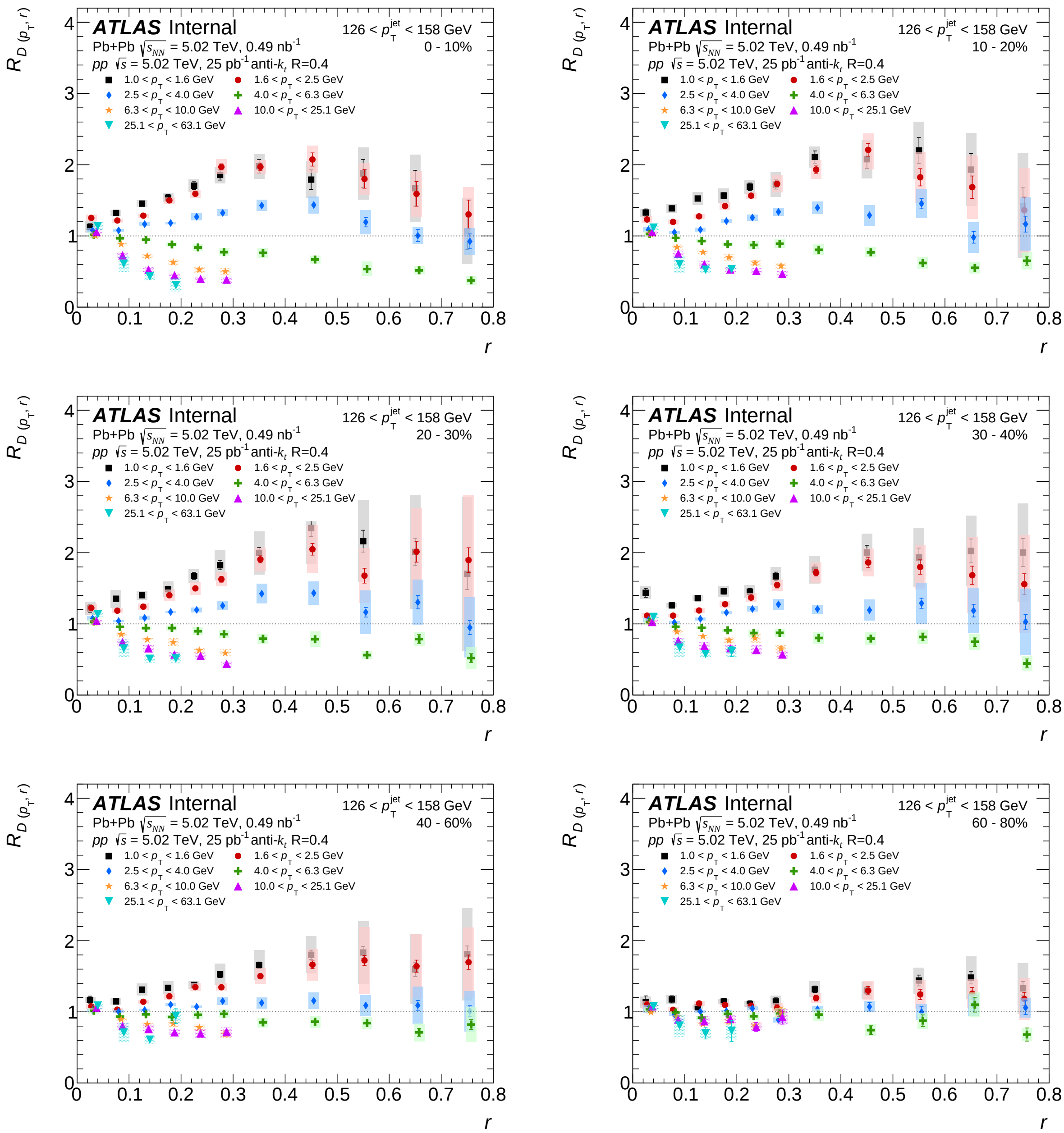

Figure 15: The $R_{D(p_{\mathrm{T}},r)}$ distributions as a function of r for different p_{T} selections in 126–158 GeV jets. The different panels refer to different centrality selections. The vertical bars on the data points indicate statistical uncertainties while the shaded boxes indicate systematic uncertainties. The widths of the boxes are not indicative of the bin size and the points are shifted horizontally for better visibility.

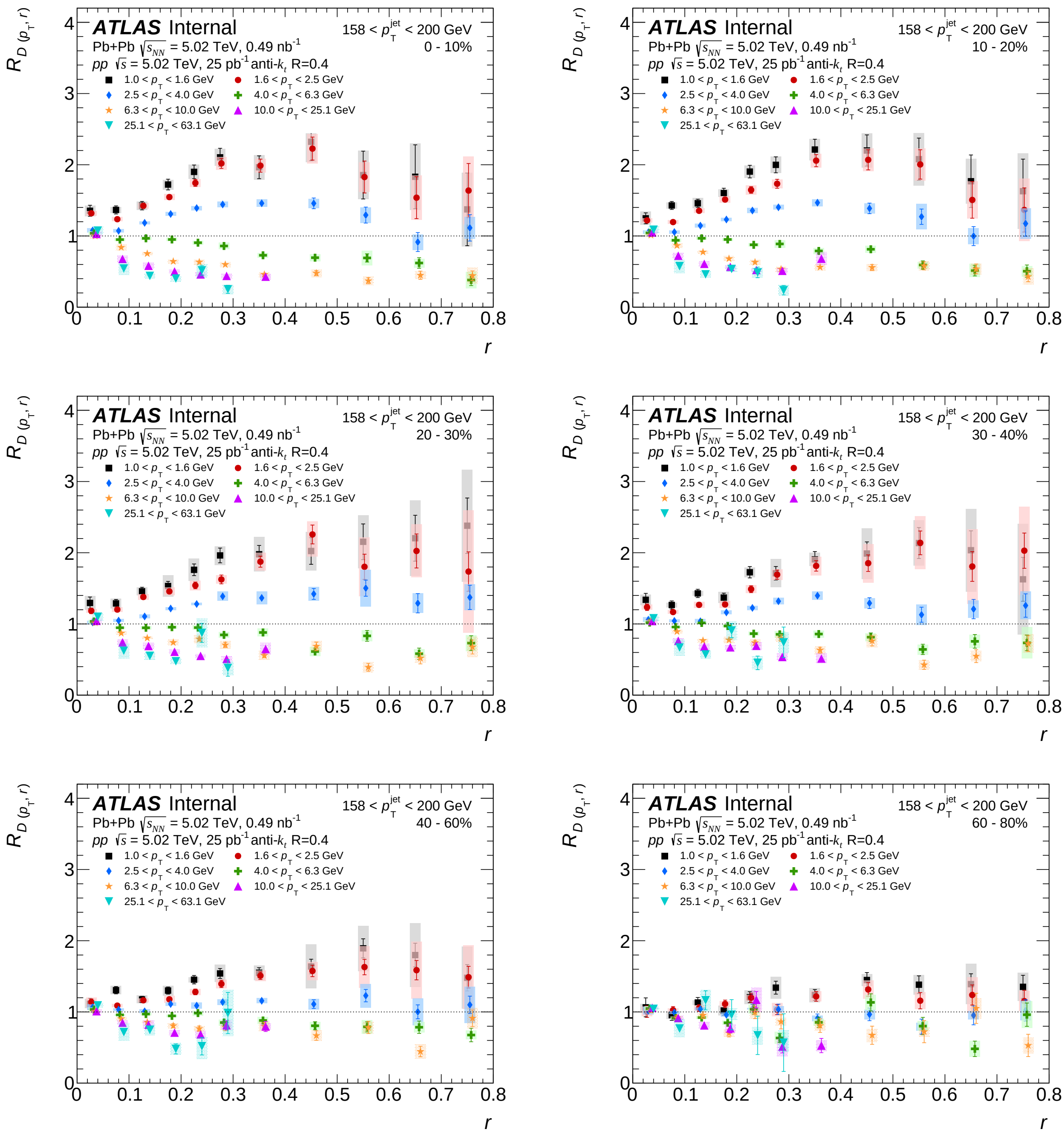

Figure 16: The $R_{D(p_\mathrm{T},r)}$ distributions as a function of r for different p_T selections in 158–200 GeV jets. The different panels refer to different centrality selections. The vertical bars on the data points indicate statistical uncertainties while the shaded boxes indicate systematic uncertainties. The widths of the boxes are not indicative of the bin size and the points are shifted horizontally for better visibility.

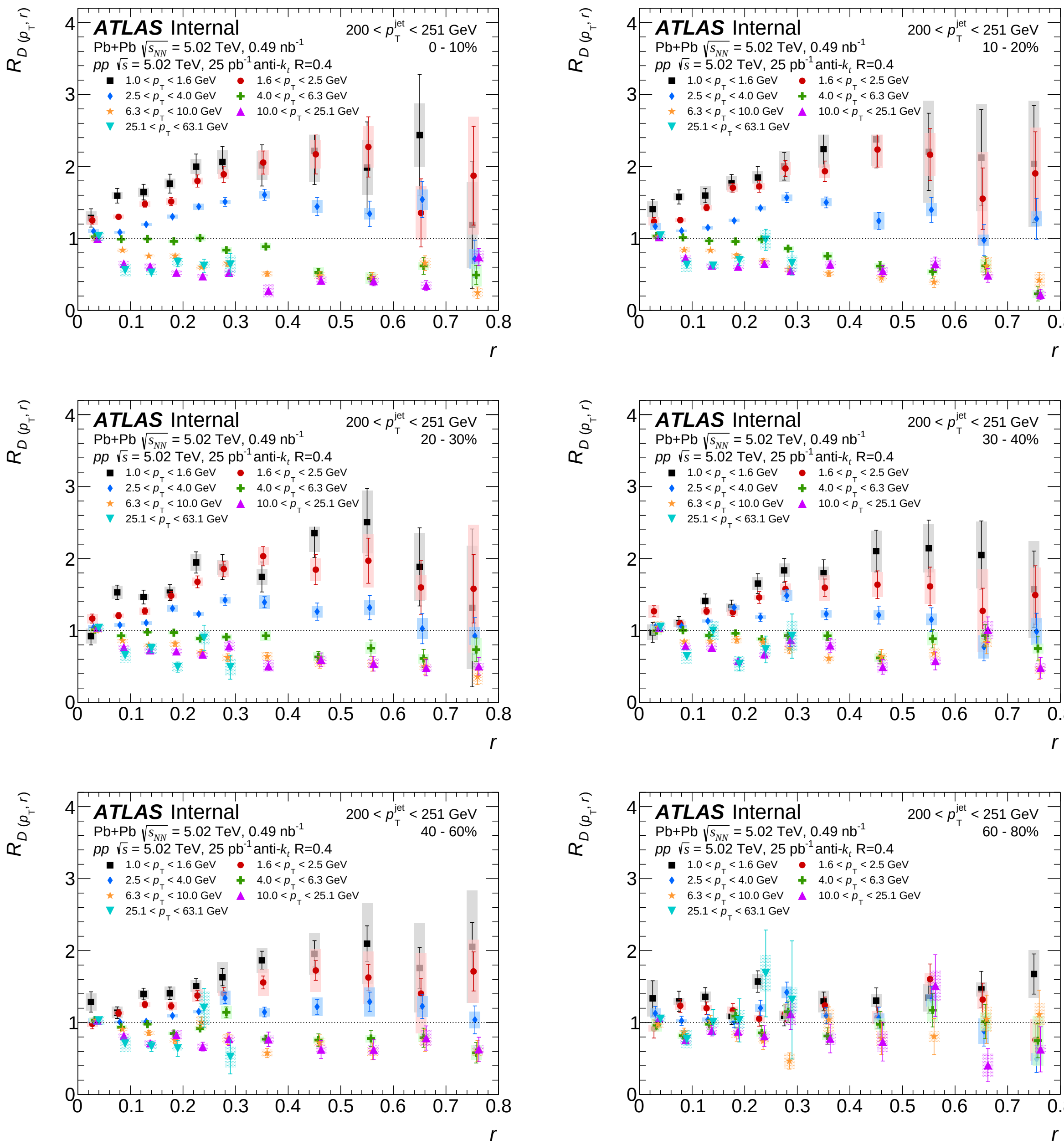

Figure 17: The $R_{D(p_{\mathrm{T}},r)}$ distributions as a function of r for different p_{T} selections in 200–251 GeV jets. The different panels refer to different centrality selections. The vertical bars on the data points indicate statistical uncertainties while the shaded boxes indicate systematic uncertainties. The widths of the boxes are not indicative of the bin size and the points are shifted horizontally for better visibility.

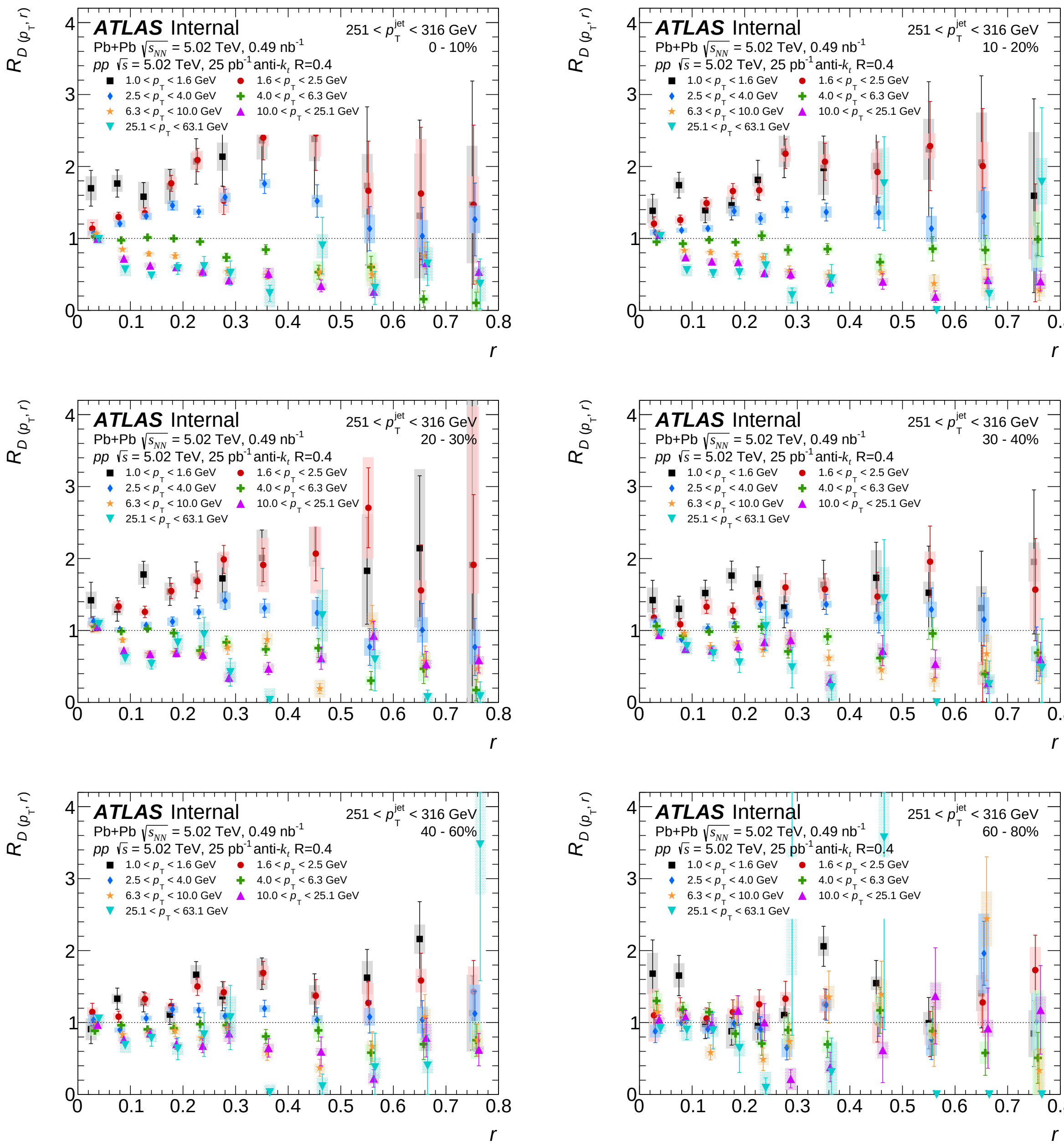

Figure 18: The $R_{D(p_{\mathrm{T}},r)}$ distributions as a function of r for different p_{T} selections in 251–316 GeV jets. The different panels refer to different centrality selections. The vertical bars on the data points indicate statistical uncertainties while the shaded boxes indicate systematic uncertainties. The widths of the boxes are not indicative of the bin size and the points are shifted horizontally for better visibility.